Development of a Catalyst Support for Fast Pyrolysis of *E. grandis* with Layered Double Hydroxides

CVD 800: Dissertation

University of Pretoria

Danya Maree

Supervisor: Prof. Mike Heydenrych

July 12, 2022

UNIVERSITEIT VAN PRETORIA
UNIVERSITY OF PRETORIA
YUNIBESITHI YA PRETORIA

Development of a Catalyst Support for Fast Pyrolysis of *E. grandis* with Layered Double Hydroxides

Synopsis

The use of bio-oil from fast pyrolysis of biomass as a substitute for conventional fossil fuels is being examined, but there is scepticism surrounding its feasibility due to its acidity, instability, and low calorific value. These characteristics are caused primarily by the high elemental oxygen content in the oil. An active catalyst which is of interest due to its reported ability to facilitate certain mechanisms favourable in oxygen reduction, is a nanostructured material called layered double hydroxide (LDH). A catalyst support was made by synthesising mesoporous silica containing pre-made MgAl-LDH and CaAl-LDH. High surface areas (up to 600 m^2/g) and mesopores (3.3 to 4.8 nm) were produced by accurate control of the synthesis pH. MgAl-LDH significantly reduced the oxygen and water contents and increased calorific values of the lighter pyro-oil fractions (16.2 to 22.5 MJ/kg), while CaAl-LDH increased the oxygen contents of these oils. The catalysts had little effect on the oxygen contents of the heavier pyro-oil fractions, suggesting that there was greater catalytic action on the lighter compounds as a result of the catalyst support pore size. The optimal catalyst support was that which was synthesized at an intermediate pH of 7. Understanding the synthesis conditions required for improved silica catalyst supports will be helpful to examine the effects of future powdered catalysts in similar processes.

Keywords: Biofuels, pyrolysis, catalysis, layered double hydroxides, nanostructured materials, porous materials

Acknowledgements

I would like to thank my supervisor, Professor Mike Heydenrych, for his guidance, support and encouragement throughout this project. I would also like to thank Professor Johan Labuschagne for providing LDHs for my experiments, as well as Hanno Muire, Ryan Merckel, Shane Tabana and Marnus Grobler, for assistance and guidance with laboratory analysis. Last, but not least, thank you to my parents, who continue to be my greatest supporters.

Contents

Synopsis i

Acknowledgements ii

Nomenclature vii

1 Introduction 1

1.1 Background 1

1.2 Problem statement and objectives 1

1.3 Method and scope 2

2 Literature overview 3

2.1 Environmental challenges in liquid fuel production 3

2.2 Fast pyrolysis of biomass main concepts 4

2.3 Fluidised bed pyrolysis reactors 6

2.4 Catalytic fast pyrolysis 7

2.4.1 Layered double hydroxides 8

2.4.2 Zeolites 11

2.4.3 Silica 11

2.5 Catalyst support design 12

2.5.1 The need for catalyst supports 12

2.5.2 Aspects of catalyst supports 12

2.5.3 Mesoporous silica as a catalyst support 13

3 Methods **16**

3.1 Materials and equipment . . . 16

3.2 Exploratory catalyst formulation . . . 16

3.3 Final catalyst preparation . . . 16

3.4 Catalyst material analysis . . . 18

3.4.1 Nitrogen physisorption . . . 18

3.4.2 Friability tests . . . 19

3.4.3 Scanning electron microscopy . . . 19

3.5 Exploratory analysis . . . 20

3.5.1 Elemental analysis . . . 20

3.5.2 TGA . . . 20

3.6 Pyrolysis . . . 20

3.6.1 Reactor set-up . . . 20

3.6.2 Reactor preparation . . . 22

3.6.3 Modifications to bench-scale reactor system . . . 23

3.7 Pyrolysis oil analysis . . . 25

3.7.1 Functional group analysis . . . 25

3.7.2 Water content determination . . . 25

3.7.3 Chemical composition analysis . . . 26

3.7.4 Bomb calorimetry . . . 26

4 Results and discussion **28**

4.1 Catalyst material characteristics . . . 28

4.1.1 Nitrogen Physisorption . . . 28
4.1.2 Scanning electron microscopy . . . 29
4.1.3 Friability tests . . . 30
4.2 Exploratory analysis . . . 31
4.2.1 Elemental analysis . . . 31
4.2.2 TGA . . . 31
4.3 Pyrolysis oil characteristics . . . 33
4.3.1 Product yields . . . 33
4.3.2 Functional group analysis . . . 35
4.3.3 Water content determination . . . 37
4.3.4 Chemical composition analysis . . . 47
4.3.5 GC/MS results compared to FTIR results . . . 50
4.3.6 Bomb calorimetry . . . 50

5 Conclusion and recommendations **51**

A Exploratory catalyst formulation **60**

A.1 Variations in concentrations of sodium silicate precursor solution . . . 60
A.2 Acid addition . . . 60
A.3 Variations in LDH loading . . . 61
A.4 Variations in gel washing procedures . . . 61
A.5 Variations in the formation of catalyst particles . . . 62

B Detailed GC/MS Results **63**

B.1 ESP oil composition 63

B.2 Heat exchanger oil organic fraction composition 63

C Python Code **66**

C.1 FTIR peak deconvolution 66

C.2 Water content determination 67

Nomenclature

BET Brunauer-Emmett-Teller

E. Eucalyptus

ESP Electrostatic precipitator

GC/MS Gas chromatography/mass spectrometry

HHV Higher heating value

LDH Layered double hydroxide

SEM Scanning Electron Microscopy

TGA Thermogravimetric analysis

W_0 Initial sample weight

W_∞ Final sample weight

X(t) Conversion of sample at time t

List of Figures

1 Powered layered double hydroxide catalyst supported by a) fine porous silica powder such as diatomaceous earth combined with a binder, and b) amorphous mesoporous silica, synthesized via the sol-gel method. 2

2 Structure of layered double hydroxides (Tabish et al., 2020). 9

3 Lignin Beta – O – 4 aryl-ether bond cleavage schematic (Lu et al., 2016). . . 10

4 Aldol condensation of furfural and acetone, catalyzed by MgAl-LDH (Hora et al., 2014). 11

5 Production of silica gel via the sol-gel process (Simatupang et al., 2018). . . 14

6 Mechanisms of hydrolysis and condensation reactions in sol-gel synthesis (Malucelli, 2016). 15

7 Photo and diagram of tail-gas recirculation spouted bed reactor (not to scale). 21

8 Tail-gas recirculation spouted bed reactor system before feed line adjustments. 24

9 (A) Catalyst support synthesis pH vs BET surface area, and (B) catalyst support synthesis pH vs BJH average pore width. 28

10 (A) A layered double hydroxide (LDH) particle, and (B) LDH flakes embedded in mesoporous silica support. 29

11 Particle of crystalline, nonporous silica (quartz) formed during support synthesis, embedded in amorphous, mesoporous silica. 30

12 Friability, defined as the % mass loss during friability tests, as a function of catalyst support synthesis pH and LDH loading (mass %). 30

13 Thermogravimetric results compared between MgAl-LDH catalyst types and support synthesis pHs. 32

14 Thermogravimetric results compared between CaAl-LDH catalyst types and support synthesis pHs. 32

15 Differential TG results compared between MgAl-LDH catalyst types and support synthesis pHs. Inflection points are indicated by the crossing red gradient lines. 33

16 Differential TG results compared between CaAl-LDH catalyst types and support synthesis pHs. Inflection points are indicated by the crossing red gradient lines. 33

17 (A) represents the change in oil, gas and char fractions with change in catalyst, and (B) represents the change in heat exchanger (HE) oil and electrostatic precipitator (ESP) oil fractions of the total oil product with change in catalyst. 34

18 FTIR spectra of (A) the Mg-Al LDH doped catalysts heat exchanger oils and (B) ESP oils, and (C) the Ca-Al LDH doped catalysts heat exchanger oils and (D) ESP oils. 36

19 Deconvolution of FTIR 1650 cm^{-1} and 3400 cm^{-1} peaks of heat exchanger oils produced without catalyst, and with silica catalyst support. (A) shows the peaks around 1650 cm^{-1} for heat exchanger oils without catalyst, and (B) the peaks around 3400 cm^{-1}. (C) shows the peaks around 1650 cm^{-1} for heat exchanger oils with silica catalyst support, and (D) the peaks around 3400 cm^{-1}. 38

20 Deconvolution of FTIR 1650 cm^{-1} and 3400 cm^{-1} peaks of heat exchanger oils produced with MgAl-LDH catalysts. (A) shows the peaks around 1650 cm^{-1} for heat exchanger oils with MgAl-LDH catalyst 1, and (B) the peaks around 3400 cm^{-1}. (C) shows the peaks around 1650 cm^{-1} for heat exchanger oils with MgAl-LDH catalyst 2, and (D) the peaks around 3400 cm^{-1}. (E) shows the peaks around 1650 cm^{-1} for heat exchanger oils with MgAl-LDH catalyst 3, and (F) the peaks around 3400 cm^{-1}. 39

21 Deconvolution of FTIR 1650 cm^{-1} and 3400 cm^{-1} peaks of heat exchanger oils produced with CaAl-LDH catalysts. (A) shows the peaks around 1650 cm^{-1} for heat exchanger oils with CaAl-LDH catalyst 1, and (B) the peaks around 3400 cm^{-1}. (C) shows the peaks around 1650 cm^{-1} for heat exchanger oils with CaAl-LDH catalyst 2, and (D) the peaks around 3400 cm^{-1}. (E) shows the peaks around 1650 cm^{-1} for heat exchanger oils with CaAl-LDH catalyst 3, and (F) the peaks around 3400 cm^{-1}. 41

22 Deconvolution of FTIR 1650 cm^{-1} and 3400 cm^{-1} peaks of ESP oils produced without catalyst, and with silica catalyst support. (A) shows the peaks around 1650 cm^{-1} for ESP oils without catalyst, and (B) the peaks around 3400 cm^{-1}. (C) shows the peaks around 1650 cm^{-1} for ESP oils with silica catalyst support, and (D) the peaks around 3400 cm^{-1}. 42

23 Deconvolution of FTIR 1650 cm^{-1} and 3400 cm^{-1} peaks of ESP oils produced with MgAl-LDH catalysts. (A) shows the peaks around 1650 cm^{-1} for ESP oils with MgAl-LDH catalyst 1, and (B) the peaks around 3400 cm^{-1}. (C) shows the peaks around 1650 cm^{-1} for ESP oils with MgAl-LDH catalyst 2, and (D) the peaks around 3400 cm^{-1}. (E) shows the peaks around 1650 cm^{-1} for ESP oils with MgAl-LDH catalyst 3, and (F) the peaks around 3400 cm^{-1}. 43

24 Deconvolution of FTIR 1650 cm^{-1} and 3400 cm^{-1} peaks of ESP oils produced with CaAl-LDH catalysts. (A) shows the peaks around 1650 cm^{-1} for ESP oils with CaAl-LDH catalyst 1, and (B) the peaks around 3400 cm^{-1}. (C) shows the peaks around 1650 cm^{-1} for ESP oils with CaAl-LDH catalyst 2, and (D) the peaks around 3400 cm^{-1}. (E) shows the peaks around 1650 cm^{-1} for ESP oils with CaAl-LDH catalyst 3, and (F) the peaks around 3400 cm^{-1}. 44

25 Fitted calibration curve of FTIR 1600 cm^{-1} water peak at different concentrations of water in ethanol, used in the determination of pyrolysis oil water contents. 45

26 GC analysis of (A) ESP oils and (B) HE oils produced by fast pyrolysis of *E. grandis* sawdust using different catalysts. 47

1 Introduction

1.1 Background

The focus on renewable energy is growing as a result of the world's increasing energy demand, the gradual depletion of fossil resources and the emissions produced by the production and combustion of fossil fuels. Wood chip waste produced in South African industries can be valorised to fuel using fast pyrolysis. Oils produced by fast pyrolysis are an interesting alternative to these fuels, because they can be produced from renewable and waste feedstocks such as sawdust, algae and plastic. The combustion of these oils also produces less greenhouse emissions. However, there is scepticism surrounding the economic feasibility of this as a result of the low quality of pyrolysis oils. The polarity, corrosiveness, instability and low higher heating value (HHV) of oils produced by fast pyrolysis of sawdust is largely as a result of high oxygen content, and makes the oils unsuitable for direct use as fuels in most applications.

Reduction of oxygenated compounds in the oils is the primary focus towards improving the oil quality. This can be achieved using an appropriate catalyst. Previous work has been done in the Department to investigate the use of layered double hydroxides (LDH) as a catalyst, due to their tunable catalytic properties and use in biomass valorisation studies. However, these studies have had limited success because LDH in its commercial powdered form cannot be directly used in pyrolysis spouted bed reactors, as a result of entrainment. Catalyst supports have thus been produced using diatomaceous earth and binding chemicals, but these supports yielded low surface areas (around 5 m^2/g) because of the binder used, namely sodium silicate. The binder yielded lower surface areas due to filling of the catalyst pores, blocking access of reacting molecules into the catalyst. Therefore, although the purpose of the binder is to strengthen the catalyst matrix, there was an interest in investigating catalyst production methods without the need for binders.

1.2 Problem statement and objectives

The number of oxygenated compounds in pyrolysis oils needs to be reduced to improve the viability of these oils as renewable fuel alternatives. Little research has been done on the ability of LDH to reduce oxygen in these oils, and even less on the effect of catalyst supports. A new catalyst support material with a high surface area is required to investigate the ability of LDH to reduce oxygenated compounds in *Eucalyptus grandis* sawdust fast pyrolysis oils.

1.3 Method and scope

Mesoporous silica catalyst supports containing LDH will be synthesised, and *E. grandis* sawdust will undergo fast pyrolysis using these catalysts in a bench-scale spouted bed reactor. Figure 1 shows how this method of catalyst preparation compares to the use of silica powder (or diatomaceous earth), LDH and a binder, in terms of the catalyst morphology. The catalyst material characteristics, including the morphology, surface area and average pore widths will be assessed. Then, the deoxygenation ability of the catalysts will be evaluated by compositional and thermal analysis of the oils produced.

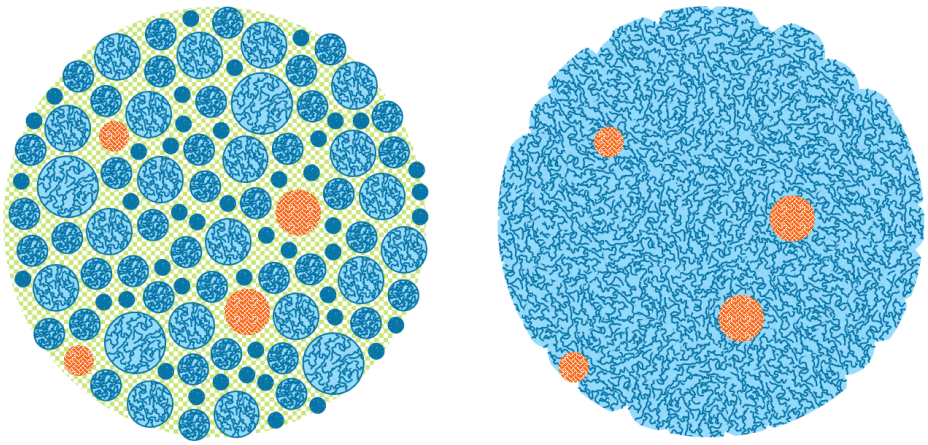

Figure 1: Powered layered double hydroxide catalyst supported by a) fine porous silica powder such as diatomaceous earth combined with a binder, and b) amorphous mesoporous silica, synthesized via the sol-gel method.

2 Literature overview

2.1 Environmental challenges in liquid fuel production

Today, around 95% of the world's oil originates from non-renewable resources such as fossil fuels (Zhang et al., 2018). Between 85 and 90% of the world's energy will continue to be from fossil fuels and non-renewable resources until 2030 (Panwar et al., 2011). Furthermore, the world's carbon dioxide emissions have been of concern for many years due to the impact of global warming. These concerns are resulting in a growing need for oil resources which are not only renewable, but produce fewer emissions.

One resource which is a promising biofuel feedstock due to its renewability and low greenhouse emissions is biomass (Sun et al., 2018). Woody biomass can be converted to pyro-oil via a process called pyrolysis, in which the feedstock is heated to high temperatures in an inert atmosphere. The oils produced contain a variety of chemicals that can be separated and sold for value, refined in petrochemical refineries, or combusted as low-grade fuels for various applications (Ratnasari et al., 2020).

Pyrolysis oil is most commonly used in boilers, diesel engines and gas turbines as fuel for electricity generation (Balat et al., 2009). However, most bio-oils today have a much lower heating value compared to classic fossil fuels such as diesel. Additionally, pyrolysis oils are corrosive, viscous and prone to coke production. Despite this, pyrolysis oil is attractive for use as a fuel because it is carbon dioxide-neutral and low in sulphur (Czernik and Bridgwater, 2004). In many cases, the use of pyro-oil produced today requires additional fuels to support start-up. Pyro-oil is a more preferred fuel feedstock than its precursor biomass because of its energy density, ease of storage and transport (Imran et al., 2018).

The most prominent challenge in the manufacturing of bio-oil from woody biomass is the chemical complexity of the oils produced (Behrens et al., 2017). Wood is comprised of cellulose, hemicellulose, and lignin, each of these comprising a high oxygen content (Chen, Che, Li, Liu, Yang, Chen, Wang, Shao and Chen, 2019). During pyrolysis, these three units convert primarily into oxygenated compounds, such as organic acids, aldehydes, ketones, alcohols, esters, etc., constituting a significant fraction of the resultant pyro-oils (Sun et al., 2020). Due to the presence of the carbon-oxygen double bonds in these functional groups, the oils are corrosive, polar, and susceptible to thermal degradation (Imran et al., 2018). More notably, high oxygen content gives the oils heating values which are approximately

half that of conventional liquid fuels (Katikaneni et al., 1995).

2.2 Fast pyrolysis of biomass main concepts

Pyrolysis is the thermal reaction of hydrocarbon-based compounds in the absence of oxygen, to form char, pyro-oil and volatile compounds at high temperatures. The main type of pyrolysis considered in this study is fast pyrolysis, classified by the following conditions (Chen, Che, Li, Liu, Haiping, Yingquan, Wang, Shao and Chen, 2019):

- High heating rates (up to 200 °C per second)
- Operating temperatures between 400 °C and 600 °C
- Residence times of less than 5 seconds
- Fast cooling of product vapours

Feedstocks are typically dried before pyrolysis to remove moisture, as heating of water is energy-intensive and does not contribute to the pyrolysis products. Drying is also necessary to remove oxygen content which causes bio-oil instability and increases viscosity, because water contained in the feedstock contributes to pyrolysis reactions that produce oxygen-rich molecules (Jahirul et al., 2016).

In addition to drying, removal of the char product is necessary because char is a catalyst that results in cracking and formation of polycyclic aromatic hydrocarbons, which increase bio-oil viscosity.

A summary of the reactions to convert lignocellulosic biomass to valuable products is given in Table 1. All undesired compounds are red, and all valuable compounds are blue. It should be noted that the undesired compounds have similarities, as do the valuable compounds. For example, undesired compounds are typically larger, more complex, and more oxygen rich, resulting in lower calorific values. Especially undesired compounds contain carbonyl groups, because carbonyl groups have a tendency to result in polymerisation (and therefore, increase in viscosity over time). The valuable compounds contain more carbon-hydrogen bonds, which are higher in calorific value.

Table 1: Characteristic reactions during pyrolysis involving cellulose, hemicellulose and lignin in biomass and their products (blue: desired products; red: undesired products)

Structural unit	Cellulose	Hemicellulose	Lignin
Depolymerisation	Sucrose, Levoglucosan	Xylose	Methoxyphenol Guaiacol
Ring-opening deconstruction	Aldehydes (hydroxyacetaldehyde, acetaldehyde)		
		Xylulose	
		Ketones (hydroxyacetone, acetone)	
Ring-opening reconstruction		Acetic acid Furfural	
		Hydroxymethylfuran, methylfurans	
Side-chain reactions			Propylphenols
			Methylcatechols Cresols
Cracking, and O and H removal	Aliphatics (alkanes, alkenes, branched hydrocarbons, cyclic hydrocarbons)		
		Phenols, cresols	
		Monocyclic aromatic compounds (toluene, benzene, etc.)	
		Polycyclic aromatic compounds (naphthalene, methylnaphthalene, etc.)	

Lignocellulosic biomass contains between 40 and 60 wt.-% cellulose, 15-30 wt.-% hemicellulose, and 10-25 wt.-% lignin depending on the source of the biomass (Behrens et al., 2017). Pyro-oil typically consists of 20-25 wt.-% water, 25-30% partially or fully decomposed lignin compounds, 5-12% organic acids, 5-10% aliphatic hydrocarbons, 5-10% sugars and 10-25% oxygen-rich compounds, such as those listed above in red (Balat et al., 2009). Its heating value is approximately 16 MJ/kg, which is about a third of that of diesel. The kinematic viscosity of bio-oil varies widely between 11 mm^2/s and 115 mm^2/s, depending on the reactions between bio-oil components during storage.

The main contributor to the problems faced with pyrolysis oil is its acid content (mostly

related to acetic and formic acid), as well as other compounds containing carbonyl groups such as ketones, aldehydes and esters. Carbonyl-containing compounds reduce bio-oil stability because they are reactive, and repolymerise over time. Lignin pyrolysis products tend to be the main contributor to this problem.

Polycyclic aromatic compounds are also undesired compounds in bio-oil, because increased compound molecular weights result in increased viscosity and therefore increased difficulty of handling. Water content contributes to lower energy density and therefore lower heating value of pyro-oil. In combustion systems, it lowers the flame temperature as a result of water's high heat of evaporation, and the fact that water does not add to the heat generation during combustion. Solid particulates such as char, ash and metals are usually present in higher quantities in pyro-oils than in conventional fuels. This results in sludge formation. Carbon dioxide, NOx and SOx emissions are lower for bio-fuels than those of conventional fuels, but particulate and carbon monoxide emissions are higher (Schwartz et al., 2020), when normalized in ppm.

2.3 Fluidised bed pyrolysis reactors

Fluidised bed reactors contain solids and pressurised fluids that, combined, behave like fluids. They are attractive for fast pyrolysis because of their high heat transfer rates (as a result of high solid-fluid surface interaction and velocity). There are a few different types of fluidised bed reactors, the main types including bubbling fluidised bed reactors and circulating fluidised bed reactors. Bubbling fluidised bed reactors typically use heated sand as the solid heat-transfer material, and are also relatively simple to design. These reactor types allow for simple building and operation, and there is increased interest in the use of catalyst particles as the fluidising mechanism (Bridgewater, 2018). The reactor contents typically move to a cyclone after the reaction to remove char. The resulting gases move into a condenser and the condensate becomes pyrolysis oil.

One advantage of fluidised bed reactors over fixed reactors is that char and tar do not accumulate in the reactor. In these reactor types, the biomass particle sizes affect the heating rates, and therefore larger costs are associated with increased grinding. Another advantage, particularly with fluidised bed reactors, is that scale-up is well-understood and easy to achieve. Spouted bed reactors are a type of fluidised bed reactor with outstanding heat-transfer between particles (Amutio et al., 2012). Circulating fluidised bed reactors allow for shorter residence times and increased throughputs with easier heating control. However,

they are more difficult to design because of the complexity of the hydrodynamics involved. Some char is also entrained in the product because of higher gas flowrates, and scale-up is not yet well-understood for this variety of fluidised bed reactors.

Recent studies have used CFD (Computational Fluid Dynamics) to predict fluid flow patterns in fluidised bed reactors during fast pyrolysis of biomass (Chen, Ku, Lin and Ström, 2020). These simulations allowed scientists to study the effects of temperature and biomass particle size on reaction kinetics and yields of certain products. With the current and new literature placing focus mainly on computational methods, there is still a lack of knowledge on the practical scale-up of these reactors (Raza et al., 2021). One study compared the results of a kinetic model generated for a micro reactor to that of a bench-scale fluidised bed reactor to gain some insight into the effect of reactor size (Hu and Gholizadeh, 2019). The result was increased decomposition of initial pyrolysis products into smaller molecules. However, more research needs to be done on pilot and industrial-scale systems, with particular focus on how designs and operating conditions of larger systems affect the pyro-oil quality.

2.4 Catalytic fast pyrolysis

One way to improve the quality of biomass fast pyrolysis pyro-oils is through the use of an effective catalyst. In a thermochemical process such as fast pyrolysis, the catalyst needs to be thermally stable, have adequate surface area and porosity (Deutschmann et al., 2011). Additionally, the selectivity of pyrolysis products varies with catalyst pore size and chemical properties of the active sites (Carlson et al., 2009). When pore sizes are too small, larger molecules undergo catalytic conversion on external sites of the catalyst, where catalytic sites are considerably fewer compared to the inner surfaces (especially for higher surface area materials), producing more undesired products in the heavier fractions (Hu et al., 2020). When they are too large, there may be more oxygenated products because of fewer overall catalytic sites (Bhoi et al., 2020). Therefore, the ability to tune the morphologies of these materials is of interest in catalysis. (Merckel et al., 2020) showed increase in the oxygen content in pyrolysis oil compounds with increasing molecular weights, as evidenced by the increased retention time in the GC/MS analysis (in a GC/MS column that separates based on molecular mass or boiling point). This is likely to be as a result of the reaction kinetics, and catalyst shape and size selectivity. In addition to larger compounds being more difficult to handle as a result of increased viscosity, their increased oxygen contents will thus lead to corrosiveness, instability and a lower HHV. This means that there is an

increased need for production and deoxygenation of smaller molecules. These results can be achieved using a catalyst with the appropriate catalytic properties, and selectivity. There are a number of minerals and nanostructured materials known for their abilities to improve pyrolysis products, including zeolites (Lappas et al., 2002), mesoporous aluminosilicates (Iliopoulou et al., 2007) and alkaline compounds (Fahmi et al., 2007).

In-situ catalytic fast pyrolysis refers to the catalytic cracking of heavier pyrolysis products into lighter compounds with higher calorific value, in the same process step as the initial pyrolysis of the biomass feedstock. This method is attractive because of its lower capital requirement (because only one reactor is needed), and easier control due to it being a simpler process (Imran et al., 2018). However, there have been recent studies conducted on staged catalysis, utilising both *in-situ* and *ex-situ* catalytic stages (Kan et al., 2020). These studies have yielded much higher (98%) oxygen removal efficiency using common pyrolysis catalysts such as HZSM-5. The major problem with the current literature on catalysts for fast pyrolysis is that the focus lies mainly on the refinement of catalysts on a laboratory and theoretical scale (Yildiz et al., 2016). There is little literature on the adaptation of catalysts for scaled-up processes, for example, consideration of durability and appropriate catalyst supports. While there is still a need for further catalyst refinement, there is also a need to find the appropriate balance of pyro-oil quantity and quality, and understand the mechanisms of the catalytic reactions (Kan et al., 2020).

An essential step to all catalytic pyrolysis research is catalyst selection. The catalyst selected needs to be capable of catalysing dehydration, decarboxylation, cracking, isomerisation, cyclisation, and depolymerisation concurrently. Before discussing the use of one type of catalytis for pyrolysis in particular, it is important to mention the different pyrolysis catalysts which are commonly used today.

2.4.1 Layered double hydroxides

A nanostructured material that has gained recent interest in biomass pyrolysis due to de-oxygenation capabilities is layered double hydroxides (LDHs) (Song et al., 2019). LDHs are a group of anionic clay compounds consisting of layers of metal hydroxides with negatively charged ions and water molecules in the interlamellar spaces, as shown in Figure 2.

LDHs have the formula $[M^{2+}_{x-1}N^{3+}_{x}(OH)_2]^{x+}(A^{m-})_{x/m} \cdot nH_2O^{X-}$, where M, N and A are divalent cations, trivalent cations and anions of various valencies, respectively. x and m define

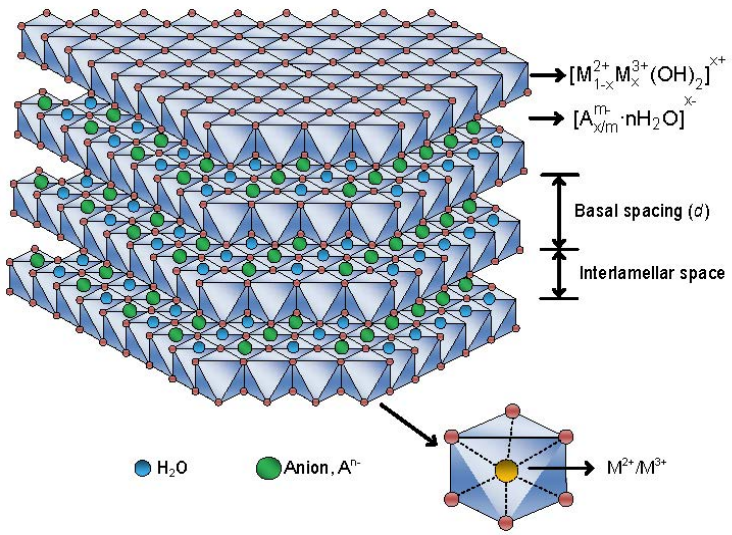

Figure 2: Structure of layered double hydroxides (Tabish et al., 2020).

the ratios of the respective ions (Wang et al., 2018). The chemical and physical behaviours, molar masses, charge densities and equivalent surface areas of LDHs, are adjustable based on the divalent (M) and trivalent (N) ions used, the ratios of these ions and the choice of interlamellar anions. LDHs have been reported to facilitate oxygen-removing reactions such as aldol condensation (Hora et al., 2014) and decarbonylation (Navarro et al., 2018). LDHs that are of interest to this study are CaAl-LDH, due to its reported aldol condensation ability (Bing et al., 2018), and MgAl-LDH, due to its popularity in catalytic biomass pyrolysis studies.

Basic catalysts, such as LDH, are of interest in biomass pyrolysis because in comparison to acidic catalysts, they are recognised for ketonization and aldol condensation reactions, which remove oxygen in the form of carbon dioxide. Reportedly, the carbon dioxide production is larger than ZSM-5. Water yield is also shown to be significantly less than when using an acidic ZSM-5 catalyst. Another important point is that LDH is cheaper than commonly available zeolites (Kalogiannis et al., 2018).

MgAl-containing LDHs are the main focus of pyrolysis catalysis using LDHs. (Navarro et al., 2018) showed that decarbonylation reactions become more prominent with an increase in the Mg/Al ratio, with all Mg-Al LDHs still producing less CO than ZSM-5. The same trend is observed for decarboxylation reactions, as the overall yield of the gaseous product tends to be higher for higher Mg/Al ratios. However, as the Mg/Al ratio increases, the bio-oil yield decreases slightly, because more of the compounds are converted to gaseous products through decarbonylation and decarboxylation reactions. As a result, the quality and stability

(oxygen content) of bio-oil improves with increasing Mg/Al ratios, at the cost of bio-oil yield. High conversions of furfural to less oxygenated products (95%) through aldol condensation has been reported to be catalysed by MgAl-LDH (Song et al., 2019).

(Merckel et al., 2020) study showed that, compared to a reference uncatalysed pyrolysis oil with a higher heating value (HHV) of 27 MJ/kg, carrying out the pyrolysis in the presence of CaAl-LDH slightly increased the HHV to 29.2 MJ/kg, while MgAl-LDH significantly increased this value to 37.3 MJ/kg (Merckel et al., 2020). The same study, as well as numerous others, demonstrated a direct correlation between elemental oxygen content and reduced HHV. Oils catalysed with MgAl-LDH were shown to contain far less oxygenated compounds. In addition, elemental analysis combined with gas chromatography/mass spectrometry (GC/MS) showed that decarboxylation was more prominent than dehydration when using CaAl-LDH.

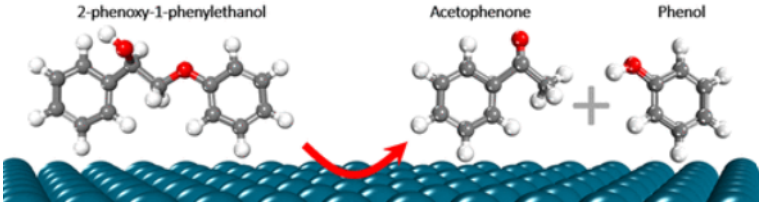

Figure 3: Lignin Beta – O – 4 aryl-ether bond cleavage schematic (Lu et al., 2016).

LDHs facilitate lignin breakdown, as it catalyses the cleavage of the – O – 4 ether bond ((Navarro et al., 2018)). This reaction is shown in 3. These bonds constitute 60 % of bonds present in lignin. A high Mg/Al ratio of MgAl-LDH catalysts relates to increased basicity (due to more basic sites), which catalyse condensation and ketonisation reactions, removing water and carbon dioxide. (Hernández Enciso et al., 2017) postulated that the breakage of the lignin Beta – O – 4 bonds may be as a result of strong basic sites (such as Mg2+) providing a binding site for the aryl ether (the oxygen linking methyl groups to the cyclic group), while the LDH interlamellar hydroxide ions catalyse the C-O bond cleavage.

Aldol condensation is an important reaction in catalytic fast pyrolysis, because the pyrolysis of lignin results in a large number of carbonyl-containing compounds which can be further deoxygenated via aldol condensation. This reaction is typically catalysed by bases such as sodium or calcium hydroxide, according to (Hora et al., 2014), but basic metal oxides and basic sites in layered double hydroxides are also capable of catalysing the reaction. An example of base-catalysed aldol condensation reaction between two model pyrolysis oil compounds, furfural and acetone, is shown in Figure 4.

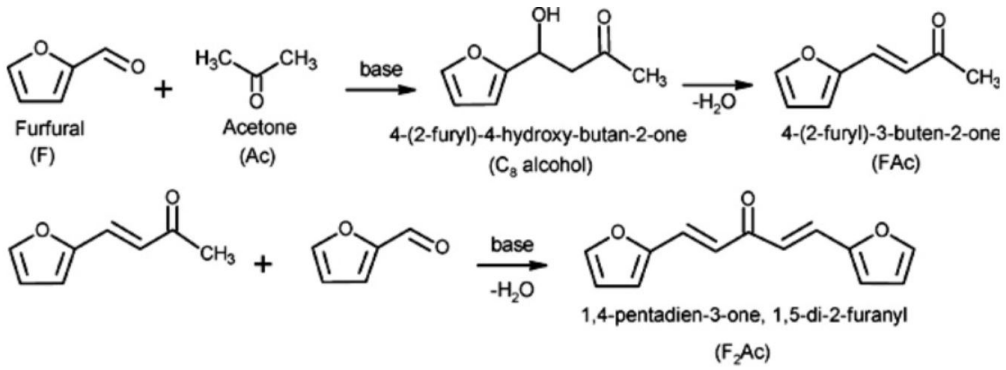

Figure 4: Aldol condensation of furfural and acetone, catalyzed by MgAl-LDH (Hora et al., 2014).

2.4.2 Zeolites

The first and most common type of catalyst is zeolites, which are a porous crystalline aluminosillicate with three-dimensional structures (Chen, Che, Li, Liu, Haiping, Yingquan, Wang, Shao and Chen, 2019). HZSM-5, for example, is commonly used in petrochemical processing for dewaxing of parrafins. Zeolites are also attractive catalysts for pyrolysis because of their acidity and selectivity, being known to remove oxygen from oxygen-rich pyro-oil components such as alcohols, acids, aldehydes and esters, typically forming aromatics. The difference in oxygen removal using an acidic catalyst such as zeolites, and a basic catalyst such as LDH, lies in the various reaction mechanisms. Acidic catalysts favour decarbonylation and dehydration reactions, whereas basic catalysts favour decarboxylation reactions (Eschenbacher et al., 2021).

2.4.3 Silica

Silica has shown to strongly interact with OH-groups in levoglucosan, one of the primary pyrolysis products of cellulose and hemicellulose. Similar to HZSM-5, silica increases coke production, particularly where pore size affects selectivity of larger phenolic compounds such as guaiacol (Behrens et al., 2017). Silica has been found to increase yields of pyro-oils containing lighter compounds, while still producing char and coke comparatively to zeolites. This is attributed to the efficient cracking of cellulose breakdown products (such as smaller acids, aldehydes and furfural) and inefficient breakdown of larger methoxyphenols. Silica is especially effective in catalysing the hydrolysis of cellulose into its base components, which are later broken down further during pyrolysis (Wang et al., 2012).

2.5 Catalyst support design

2.5.1 The need for catalyst supports

The active catalysts mentioned above have clear potential in the upgrading of pyrolysis oils, especially reduction of oxygen content. However, literature on LDHs such as MgAl- and CaAl-LDHs in fast pyrolysis in fluidised bed reactors is still limited, and there is not sufficient information on their viability. This is largely as a result of physical limitations, such as the inability to use powdered catalysts directly in a fluidised bed reactor. Therefore, it is necessary to assess the effects of these catalysts in conjunction with catalyst supports, in order to investigate the use of catalysts in scaled-up pyrolysis processes.

2.5.2 Aspects of catalyst supports

The most commonly used supports include alumina, silica, diatomaceous earth (consisting of mostly silica), porous glass, aluminosilicates, activated carbon, titania, zinc oxide and silicates (Deutschmann et al., 2009). A catalyst support used in biomass fast pyrolysis must be able to withstand temperatures higher than 500 °C. Support materials should also be optimised for the tensile strength required to withstand potential mechanical force during manufacturing, and hydraulic forces during use in reactions. Some of the factors influencing the choice of catalyst support materials are

- Tensile strength
- Resistance to attrition
- Surface area
- Porosity

Apart from changing catalyst efficiency, fracture of catalyst particles leads to process issues such as high reactor bed pressure drop, blockage and fouling, and unpredictable changes in mass and heat transfer (David, 2015). Powderising of catalyst particles can also lead to environmental hazards, as these powders may be easier released into the environment.

The method ensures self-assembly of particles into structured clusters (de Jong, 2009). Clustering of particles is as a result of weak noncovalent interactions such as van der Waals,

electrostatic, hydrophobic and hydrogen interactions. These bonds are strengthened by surfactants, neutral amines or block copolymers. Some mesoporous silicas include MCM-41, FSM-16, SBA-3 and SBA-15. The material is comprised of non-uniformly organised siloxane bridges and some silanol groups.

Recent studies have developed catalyst supports that are refined for specific reaction types such as decarboxylation, hydrodeoxygenation and decarbonylation (Goh et al., 2021). Zeolite and oxide supports are commonly used for this purpose. More recent studies are focused on computational methods of optimising catalyst supports. These methods range from DFT (Density Functional Theory) simulations of the catalyst support production itself, to the catalytic mechanisms, to catalyst activation (Corral Valero and Raybaud, 2020).

The method of forming usable catalyst particles containing LDH was considered in this study. Other studies have produced LDH catalyst pellets via spray-drying, but these methods have produced pellets with surface areas which are low (around 40 m^2/g) (Wang et al., 2008), compared to mesoporous silica (500 m^2/g) (de Jong, 2009). In addition, spray-drying requires additional steps such as calcination and rehydration.

The catalyst support considered in this study is mesoporous silica, due to its high surface area per unit mass, consistently sized pore passages, abilitiy to control the quantity siloxane and silanol active sites, hydrothermal robustness (Wei et al., 2022), and the ability to control its morphology during synthesis (Fotoohi et al., 2018). The morphology of mesoporous silica is sensitive to its reaction conditions. This is as a result of the two mechanisms which occur during the polymerisation reaction resulting in the formation of mesoporous silica, namely condensation (the combination of silicate ions to form siloxane chains) and hydrolysis (the termination of silicate ions to form silanol groups) (Schubert and Hüsing, 2019). The rates of the respective reactions are dependent on the synthesis pH. This results in varying material properties, including surface areas and pore sizes (Ko, 1999). Although silica has been reported to show some catalytic activity as a result of weak acidic sites (Behrens et al., 2017), its effect on pyrolysis products is small, and it can therefore be used as a catalyst support to investigate the catalytic effects of LDHs.

2.5.3 Mesoporous silica as a catalyst support

Mesoporous silica is a synthetic form of silica produced using sol-gel synthesis. The sol-gel reaction process is shown in Figure 5. It is associated with high surface area per unit

mass (approximately 500 m^2/g) and the production thereof is favoured for control over its composition and morphology (de Jong, 2009). The sol-gel process, which can also be used to develop gels from other compounds such as those containing metal atoms, and will be discussed in more detail in following sections. The pH of polycondensation has a direct effect on the branching of the gel obtained by sol-gel synthesis. The porosity of silica gel is usually greater than 90 % and the thermal conductivity is low (0.014 W/m.K). The drawback of using silica gels in catalysis is that they possess low mechanical strengths. For this reason, other materials are sometimes used to improve their mechanical properties (Amonette and Matyas, 2017).

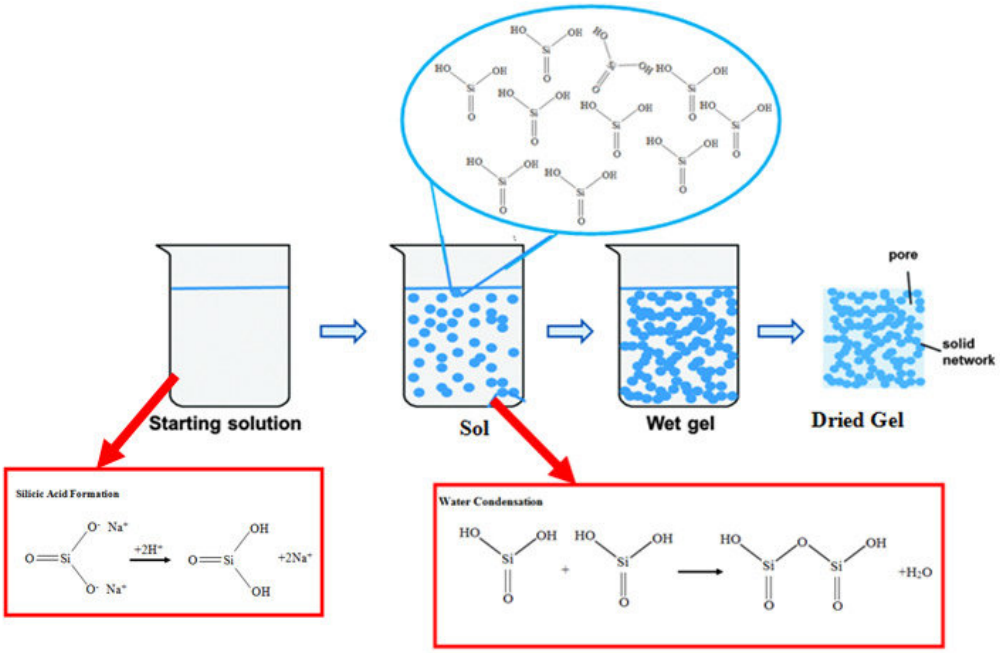

Figure 5: Production of silica gel via the sol-gel process (Simatupang et al., 2018).

As previously mentioned, the porosity of the resulting silica gel is a direct result of branching during the hydrolysis and condensation process. At a high pH, the resulting gel is highly branched, because the condensation rate is greater than the hydrolysis rate. This results in larger pores. The mechanisms of these reactions are shown in Figure 6. The factors influencing the dominance of hydrolysis over condensation and vice-versa are discussed (Schubert and Hüsing, 2019).

When the mixture pH is lower, more Si-OH (silanol) groups are produced because hydrolysis is favoured. This results in the formation of more new monomers. When the pH is higher, these silanol groups are more readily used in condensation reactions, forming more siloxane

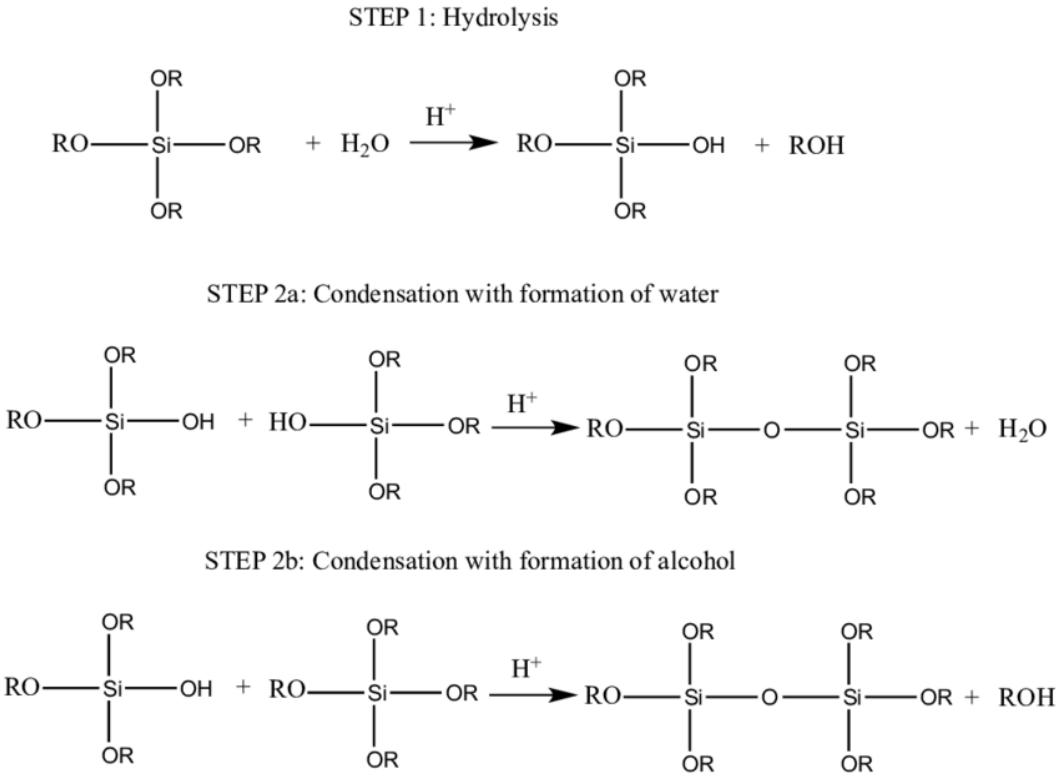

Figure 6: Mechanisms of hydrolysis and condensation reactions in sol-gel synthesis (Malucelli, 2016).

groups and thus longer branches. Therefore, siloxane bonds are more readily broken.

For each precursor solution, there is a specific pH at which a silica sol is stable, meaning that the silica particles repel one another due to their electrostatic charge, and form a stable suspension. When sodium silicate is used, the stable pH (known as the isoelectric point) is approximately 2. Below this pH, the silica particles are positively charged and they form a stable suspension. At a pH of around 4, they have almost no charge and begin to form silica chains with very little three-dimensional linkage. As the pH increases up to 8, the particles are negatively charged and once again repel one another to form a stable solution. At a pH of 8 and above, the particles once again bind to one another, but with an increased concentration of three-dimensional linkages.

3 Methods

3.1 Materials and equipment

Materials for catalyst development include sodium silicate pentahydrate and sulfuric acid purchased from Chem Lab Supplies (Johannesburg, South Africa), MgAl-LDH with a 2:1 Mg/Al ratio with CO_3^{2-} interlamellar ions are sourced from the Institute of Applied Materials at the University of Pretoria (Pretoria, South Africa), and CaAl-LDH with a 2:1 Ca/Al ratio with CO_3^{-} interlamellar ions are sourced from Greenfield Additives (Pretoria, South Africa). Mixed *E. grandis* waste chips are sourced from SAPPI South Africa.

3.2 Exploratory catalyst formulation

Before the final catalyst support preparation method was developed, several methods of preparation were explored. Explored methods included different methods of silica gel support synthesis, support to LDH ratios, formation and processing of catalyst particles. Methods were rejected on a trial-and-error basis. A summary of these methods, as well as reasons for rejection, are given in Table 2. An in-depth expansion on these methods and their outcomes is presented in Appendix A.

3.3 Final catalyst preparation

The CaAl- and MgAl-LDHs are sieved to below 38 μm. A sodium silicate solution is prepared by mixing 70 g sodium silicate pentahydrate with 725 g deionised water and stirred vigorously at 50 °C using a magnetic hotplate stirrer until dissolved. Three quantities of 0.4 g, 1 g or 2 g of sieved LDH are added and the mixture is stirred vigorously for 5 minutes to ensure an even suspension. These quantities are chosen because they are within the same ratios of other similar catalysts and their supports. The 2 g LDH samples are used for reactor and oil experiments because they contain the maximum LDH loadings, while the smaller LDH concentrations are only used to examine the effects of LDH loadings on particle friabilities. While stirring vigorously and monitoring the pH, a 1:4 solution of sulfuric acid are slowly added to the mixture. At a pH of around 9.4, the mixture begins to polymerize and is stirred until a smooth slurry is formed. Acid is then added slowly until pHs of 9, 7 and 5 are achieved, storing thirds of the slurry in Schott bottles at the respective pHs. The slurries

Table 2: Exploratory catalyst support preparation methods, and reasons for method rejection or adjustment

Preparation method	Reason for rejection	Adjustment
Sol-gel synthesis		
Saturated sodium silicate solution (20%) used as a precursor	Produced brittle gels	Reduced precursor concentration to 1%
Dilute (1%) sodium silicate precursor solution used	Yields small amount of silica gel	Increase precursor concentration to 9%
Concentrated acid added	LDH dissolved, as evident by carbon dioxide bubbles	Reduce acid solution concentration to 20%
Acid added to solution all at once, without pH control	Hard, brittle solids formed instead of gel	Acid added dropwise, to pHs of 9, 7 and 5
Support to LDH ratio of below 1:1 used	Soft, brittle gels formed	LDH ratios of below 20% used
Gels washed immediately after synthesis	Produced brittle gels	Gels left to age for 30 minutes after synthesis
Particle processing methods		
Gels strained and formed into lines, and chopped into pellets	Inefficient	Forming replaced by gel droplets
Droplets of gel onto plastic sheets to form droplet-shaped particles	Droplets flattened during drying	Droplets replaced by extrusion
Extrusion of gels through syringe, followed by chopping into pellets	Time-consuming	Extrusion replaced by forming of pellets by rolling gels on rotary shaker
Spraying extruded particles with binder (saturated sodium silicate solution)	No effect	Step removed
Oven-drying particles	Dried particles were more brittle than without oven-drying	Particles air-dried
No washing of gels after synthesis	Gels crumble during drying due to formation of salt crystals	Round of washing every two days after synthesis
Calcining at various temperatures between 500 and 800 °C	Particles became brittle	Calcining step removed

are stored for 30 minutes and then filtered and washed 5 times with 200 ml deionised water at room temperature. The paste-like slurries, which are about 3 cm thick, are stored in open aluminium tins to airdry in a temperature and humidity controlled laboratory for 4 days (20 °C and 56% respectively), with five rounds of washing with deionised water taking place every second day to remove remaining water-soluble salts.

Overall, 7 catalysts are produced for reactor experiments: 10% MgAl-LDH supported by mesoporous silica synthesized at pHs of 5, 7 and 9, 10% CaAl-LDH supported by mesoporous silica synthesized at pHs of 5, 7 and 9, and mesoporous silica reference catalyst containing no LDH, synthesised at a pH of 7. On the 4th day of drying, the slightly soft gels are broken into small sizes (approximately 4 mm), placed on a 3 mm, 1.5 mm and 0.5 μm sieves stacked on one another, and the sieves are secured on a rotary shaker. The shaker is operated at 290 rpm for one minute or until the gel pellets are roughly spherical. The pellets, sized between 0.5 μm and 3 μm, are then set to air-dry in the laboratory until completely hardened, and stored in containers to await characterisation. After drying (and significant particle drinkage), each set of catalyst particles is sieved to between 0.8 mm and 1.2 mm, the size range required for the spouted bed reactor. Any particles smaller than this, which are now essentially powders, are kept for TGA experiments.

3.4 Catalyst material analysis

3.4.1 Nitrogen physisorption

A Micromeritics TriStar II Plus BET Surface Area Analyser is used for Brunauer-Emmett-Teller (BET) analysis. N_2 gas, a temperature of 77K, and a p/p_0 range between 0.05 and 0.35 are used. Approximately 2.5 ml of each sample is placed in a BET analyser tube. The tubes are placed in the degasser at 110 °C and under vacuum to remove water, volatiles and organic impurities for approximately 10 hours until a full vacuum is established. The instrument software is then used to run the analysis, and the BET surface areas and BJH average pore widths are determined using the software. Samples synthesized under the same conditions are tested in triplicate to ensure repeatability of data.

3.4.2 Friability tests

Friability is the measure of how much mass is lost by a solid particle as a result of abrasion. In a fluidised bed, the catalyst particles are expected to experience abrasion by the movement of the fluidising medium (sand). This abrasion is simulated during friability tests. A quantity of 250 g sand sieved to between 0.8 mm and 1.2 mm, the same size sand as used in the fluidized bed reactor, are placed on a 212 μm sieve. The pool filter sand used has a hardness of 7/10 (Moh's hardness scale), sourced from a South African pool filter sand provider, and comprised of crystalline silica. Catalyst particles are sieved to between 2.4 mm and 3 mm. The assumption is that because the morphology of silica should be uniform, the percentage of abrasion is independent of particle size. About 0.5 g of the sieved catalyst is weighed and placed on top of the sand. The 212 μm sieve is placed on the rotary shaker and shaken at 290 rpm for 5 minutes. 5 minutes is chosen, because it is just long enough to sustain a significant effect from the abrasion, and is close to the amount of time that the reactor runs during a single pyrolysis experiment. After shaking, the catalyst particles that remain above 1.7 mm are sieved out and weighed. The percentage mass loss is calculated as the percentage difference between mass after shaking and before shaking. These percentages are recorded for each synthesis pH, and LDH loadings of 2%, 5% and 10%. Three runs are recorded for each of these conditions.

3.4.3 Scanning electron microscopy

Small amounts of powdered sample, prepared by crushing particles from the reactor experiment sample sets in a mortar and pestle, are sieved to below 75 μm. The powders are pressed onto double-sided tape and the excess is blown off using a high-pressure nitrogen nozzle. Each piece of sample tape is pressed onto a metal plate and coated with carbon. Images are captured using a Zeiss 540 Ultra FEGSEM at magnifications between 8K and 50K times. The EHT (electron high tension) is 2 kV and the scan speed is 9.

3.5 Exploratory analysis

3.5.1 Elemental analysis

Elemental analysis is performed on a *E. grandis* sawdust sample by the Department of Chemistry, University of Pretoria. Analysis is done on a Thermo Scientific Flash 2000 Organic Elemental Analyser, to determine carbon, hydrogen, nitrogen and sulphur mass percentages. The oxygen mass percent is estimated as the residual.

3.5.2 TGA

TGA is an important technique of measuring the effects of temperature, heating rate, atmosphere and use of catalysts on biomass constituents (Ong et al., 2020). The output of TGA is a sample weight-time curve during isothermal or changing temperature conditions. The conversion is the sample is given by the following equation (Amutio et al., 2015).

$$X(t) = \frac{W0 - W(t)}{W0 - W\infty} \tag{1}$$

Where X is the conversion of the sample at time t, W_0 is the initial sample weight, and W_∞ is the final sample weight.

A PerkinElmer TGA 4000 is used for TG analysis. Samples consisting of 2 mg catalyst ground to 125 μm, and 8 mg *E. grandis* sawdust sieved to 250 μm, are loaded into each crucible. A N_2 gas flow rate of 200 ml/min is used. A sequence intended to simulate fast pyrolysis is set to run. This includes a ramp to 105 °C at 50 °C/min to dry the specimens, and a ramp to 900 °C at 500 °C per minute.

3.6 Pyrolysis

3.6.1 Reactor set-up

A tail-gas recirculation fast pyrolysis reactor, as shown in Figure 7, is used to investigate the effects of each catalyst. The length, top and bottom diameters of the reactor itself are 0.8 m, 0.15 m and 0.1 m respectively. The sample feed tube length is 0.4 m, and the heat exchanger

length is 0.6 m. The electrostatic precipitator (ESP) comprises of an enclosed perspex tube with a diameter of 0.2 m, with a metal rod of a length of about 0.3 m suspended in the centre.

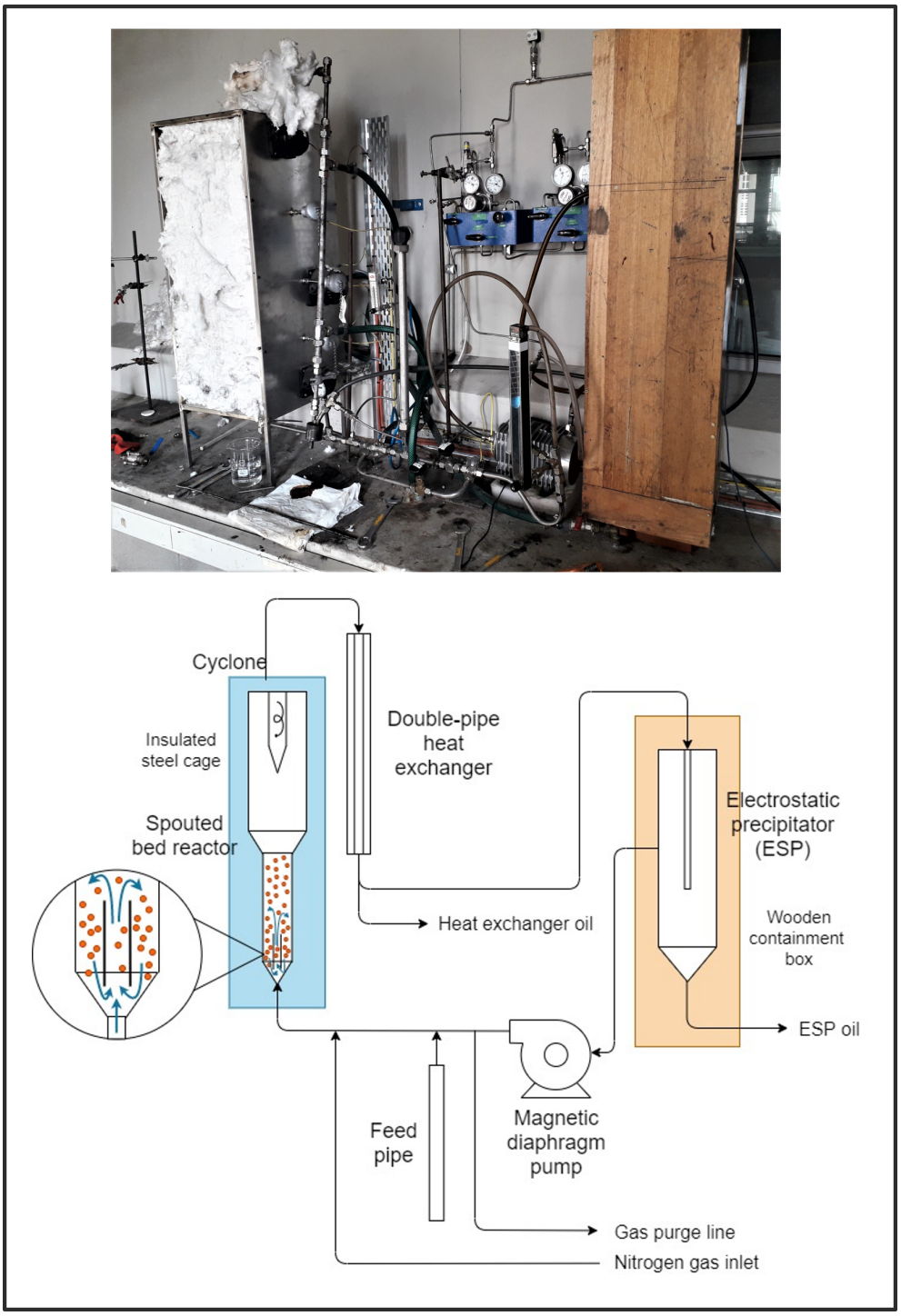

Figure 7: Photo and diagram of tail-gas recirculation spouted bed reactor (not to scale).

3.6.2 Reactor preparation

Mixed *E. grandis* sawdust sieved to between 150 μm and 300 μm is dried in a convection oven at 105 °C for one hour. To prepare the reactor system, the piping and process equipment internal surfaces are cleaned using acetone and soap water. Two 250 ml and 150 ml Schott bottles are screwed onto the oil collection ports of the heat exchanger and electrostatic precipitator (ESP) respectively. The reactor base is screwed open and the previous heat transfer medium and/or catalyst particles are allowed to pour out and were stored, after which the reactor based is screwed closed. A 1:4 volume/volume ratio of catalyst particles to heat transfer medium (pool filter sand sourced from a South African supplier) totalling 100 ml, both of which were sieved to between 0.8 mm and 1.2 mm, are poured into the top of the reactor, and the top of the reactor is closed. The pump is switched on to ensure that the reactor bed is fluidising, as indicated by a negligible increase in the pressure before the reactor upon increasing the gas velocity (and thus a negligible increase in the pressure drop over the bed). A flowmeter reading of at least 50 l/min before the feed pipe is required. Soap water spray is used to ensure that the system is free of leaks. The reactor top and bottom heating elements are then switched on and set to 600 °C, and the reactor is purged with nitrogen gas.

Reactor operation Once the temperatures has stabilised at 600 °C, the nitrogen purge gas is closed and the ESP is switched on. The feed pipe is filled with 100 g dried sawdust, screwed closed and the downward tilt of the pipe is adjusted to approximately 45°. The pump is switched on, and the sawdust is allowed to fall into the process line via vacuum. The sawdust continues into the fluidised bed, where it is pyrolysed. The pyrolysis vapours flow through a double pipe heat exchanger configured in a counter-current flow, where those vapours condensed at an inner tube product temperature above 70 °C are collected in the 250 ml Schott bottle. The flow rate is manually adjusted to maintain this product temperature, as monitored using a temperature gun. Pyrolysis char is collected in the cyclone, which is located in the reactor disengagement zone. A small amount of fine char estimated at 3 g gathered in the piping between the reactor and the heat exchanger, and is taken into account in yields calculations. Remaining condensable vapours travel through the ESP and are collected in the 150 ml Schott bottle. Non-condensable gases travel out of the gas purge line and through a ventilation line. Once the sawdust is depleted, as evidenced by no more smoke flowing into the 250 ml Schott bottle, the pump is switched off, the feed pipe refilled and closed, and the pump is switched on. The process is repeated until a total of 100 g of sawdust has been used, which takes approximately 5 minutes. For each run, 100 g sawdust

is used, and 3 runs are completed per catalyst to ensure repeatability of data. The gas pressure remain constant throughout each run, and the non-condensable gases are purged into an overhead ventilation system. To provide a reference, 3 runs without catalyst are also completed.

The heat exchanger and ESP oil yields are measured by weighing the respective Schott bottles before and after the experiments. The char yield is determined by removing the cyclone separator from the reactor after each experiment (once the reactor had cooled), unscrewing the end of the cyclone, and pouring its contents into a beaker. The beaker containing char is then weighed. The gas yield is determined as a mass difference between the feed, the oil and the char yields.

3.6.3 Modifications to bench-scale reactor system

During the exploratory bench-scale pyrolysis experiments, it was found that there were practical issues in the reactor system. The initial system, before any adjustments, contained a feed line with two ball valves, and a bypass line with a gate valve, across the feed line. This is shown in Figure 8. During reactor operation, the feed line valves were closed and the bypass valve opened while the feed pipe was filled. Once the feed pipe was filled, the feed line valves were opened. The bypass line remained open to allow for flow in case of blockages in the feed line.

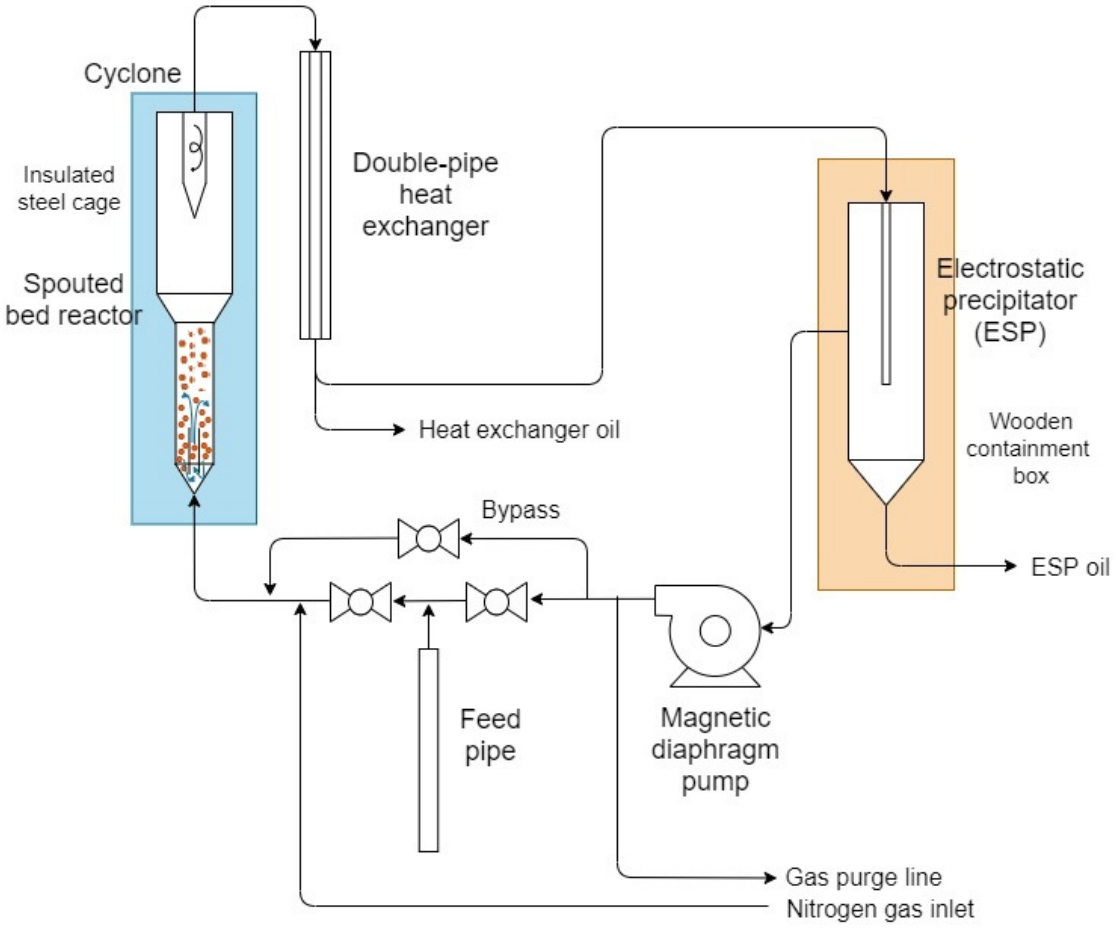

Figure 8: Tail-gas recirculation spouted bed reactor system before feed line adjustments.

Although this arrangement allowed for the feed pipe to be filled while the pump was on, there were severe difficulties with sawdust blockages and compacting inside the valves and bypass-to-feed line connections. This was as a result of the small line and connection inner diameters, and the tendency of sawdust to clump and form bridges. Pressure drops were created by even small sawdust blockages, as well as the extra connections. This restricted flow to the reactor, producing plug flow in the reactor bed, increasing the reactor residence time, and reducing the flow through the cyclone and condenser. When this happened, the quantity of oil collected was greatly reduced, and tar formed in all of the piping, including the pump. There was also a greater tendency of the piping between the cyclone and condenser to be blocked by tar.

The frequency of blockages was greatly reduced by removing the bypass line, as shown in Figure 7. This reduced pipe length and connection points, which also reduced the total pressure drop. The drawback of this system is that the pump needs to be switched off when

the feed pipe is filled, and switched back on during pyrolysis.

3.7 Pyrolysis oil analysis

3.7.1 Functional group analysis

A PerkinElmer FTIR spectrometer is used for the analysis. The FTIR software is used to run a background test, and a drop of oil sample is placed on the analyser crystal. The arm is placed over the crystal and fastened. Wavenumbers 4000 cm^{-1} through 400 cm^{-1} are analyzed using the software, and this provides a spectrum of peaks. The respective peak areas of each sample are compared to those of the reference samples (heat exchanger and ESP oils using no catalyst, and silica catalyst support).

3.7.2 Water content determination

The ATR-FTIR spectra produced are analysed to determine water content, using peak deconvolution and calibration curve fitting. Peak deconvolution is the separation of two or more overlapping peaks in spectra such as FTIR, to allow for analysis and quantification of the individual peaks. Water calibration solutions are produced by FTIR analysis of 10%, 25%, 50%, 75%, 90% and 100% water in ethanol (W/W). Ethanol is chosen as the second component, because it does not have a peak at 1600 cm^{-1}. This peak can therefore be used for water content determination without the need for deconvolution of the calibration solution FTIR spectra, which will increase accuracy. A calibration curve is also generated for the 3000 - 3600 cm^{-1} range, bearing in mind that alcohol is also a contributor to this peak. The calibration in this peak is therefore used as a verification of the results from the 1600 cm^{-1} peak, rather than being used on its own for the calibration curve. The calibrations are verified by checking if the ratio of the 3000 - 3600 cm^{-1} peak to the 1600 cm^{-1} peak is consistent for each sample analysed. A water concentration vs. peak area curve is fitted for the two peaks. A Python curve-fitting algorithm is then used to deconvolute the overlapping peaks around these wavenumbers for each oil, according to Gaussian distribution curves. This code is presented in Appendix C. The bond vibrations responsible for the separated peaks are identified according to Table 3 (Pedraza et al., 2014), (Silverstein et al., 2005). The water peak areas are compared to the concentration vs. peak area curve to find the water concentration.

Table 3: FTIR wavenumber ranges of peaks associated with and surrounding water bond vibrations

Wavenumber range	Functional Group
3200-3600	H-bonded O-H stretch (water)
3100-3500	Free O-H stretch (alcohols)
2800-3100	C-H stretch (alkanes)
1670-1820	C=O stretch (carbonyl group)
1600-1700	-OH bending (water)
1500-1650	C=C stretch (alkenes)

3.7.3 Chemical composition analysis

GC/MS is used for chemical composition analysis. ESP oils do not require sample preparation for GC/MS, as they are already in organic phase. The heat exchanger oil components are almost completely aqueous because of their polar nature, meaning that they required extraction into an organic medium before they can be analyzed using GC/MS. Organic constituents in the heat exchanger oils undergo liquid-liquid extraction using a 1:2 ratio by mass of oil to ethyl acetate, 15 min of vigorous stirring, and two days of phase separation. The ESP oils, and ethyl acetate phases of the heat exhanger oils, are used for GC/MS analysis. GC/MS is performed on the pyrolysis oils using a PerkinElmer Clarus 600 Gas Chromatograph with a 5MS capillary column (helium as the carrier gas) in split-less mode, and a PerkinElmer Clarus 600T Mass Spectrometer. About 2 μl sample is injected into the injector port, and the injector temperature is set to 250 °C. The initial oven temperature is set to 50 °C for 5 minutes, and then rises to 250 °C over 10 minutes, holding 250 °C for a further 5 minutes. Mass spectra are gathered in total ion current (TIC) mode for molar masses from 30 to 300. Compounds are determined using the NIST11 library.

3.7.4 Bomb calorimetry

The samples are prepared by mixing a 4:1 mass ratio of ESP oil samples with ethanol to aid combustion. A Parr Calorimeter 6200 is used with a 1104 Oxygen Combustion Bomb. The instrument water bucket is filled with the required amount of distilled water, and the sample is poured into a crucible and the mass of both the sample and the added ethanol is measured. A nichrome fuse wire is threaded through the instrument sample holder and through the sample, ensuring that the wire does not make contact with the surfaces of the

crucible. After the holder is placed in the bomb, it is pressurised with oxygen at 3 MPa. The bomb is then placed in the water bucket, the wires connected and the program is run. A current is run through the wire to ignite the sample, thereafter the amount of heat transferred to the water bath is determined via the temperature difference. The instrument uses this temperature difference to determine the higher heating value (HHV) of the sample in MJ/kg to 3 significant figures, taking into account the energy released by the nichrome wire. The HHV of the ethanol is taken into account to determine the HHV of the oil, and is calculated using 2.

$$HHV_{Pyro-oil} = (HHV_{Total} * m_{Total} - HHV_{EtOH} * m_{EtOH})/m_{Pyro-oil} \tag{2}$$

4 Results and discussion

4.1 Catalyst material characteristics

4.1.1 Nitrogen Physisorption

After quantification of the BET surface area and BJH adsorption average pore width of each of the 10% LDH catalyst samples, it was found that the average BET surfaces areas were 610, 522 and 381 m^2/g for catalysts synthesized at pHs of 5, 7 and 9 respectively. This is shown in Figure 9. The BET surface areas of MgAl-LDH and CaAl-LDH are 18 m^2/g and 5 m^2/g respectively (Labuschagne et al., 2019). The downward trend in surface area is contrasted by an upward trend in BJH average pore widths, shown by values of 3.3, 4.0, and 4.8 nm for the respective synthesis pHs.

This relationship is shown in Figure 9. The higher proportion of condensation reactions and thus silica chain growth at higher pH, and lower proportion of hydrolysis reactions and thus silica branch formation at lower pH, are likely to be contributing factors for the differing material characteristics.

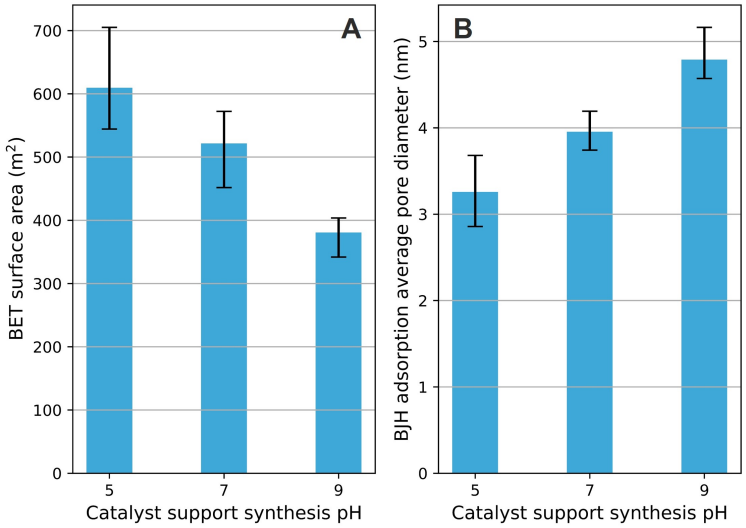

Figure 9: (A) Catalyst support synthesis pH vs BET surface area, and (B) catalyst support synthesis pH vs BJH average pore width.

These values are consistent with those reported in literature synthesised at similar conditions, which are within ranges of 400 and 850 m^2/g for surface area, and 3 and 5 nm for average

adsorption pore width (Kumar et al., 2018) (Kurdyukov et al., 2015). Reported surface areas of other pyrolysis catalysts include 460 m^2/g for HZSM-5 and 188 m^2/g for alumina (Luna Murillo et al., 2020). Although the active surface area of LDH itself is important, the surface area of the catalyst support is of primary concern, because it is an indication of the number of active sites of smaller LDH particles that are spread out and embedded within its matrix.

4.1.2 Scanning electron microscopy

Figure 10 shows the morphology of LDH as well as flakes of LDH embedded in the catalyst support. The mesoporous silica has a rough but homogenous texture, while the LDH consists of relatively smooth, rounded flakes.

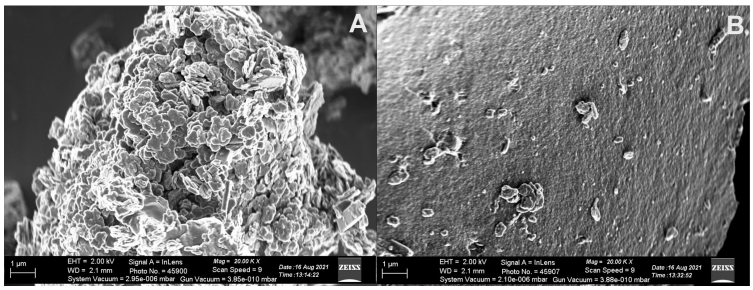

Figure 10: (A) A layered double hydroxide (LDH) particle, and (B) LDH flakes embedded in mesoporous silica support.

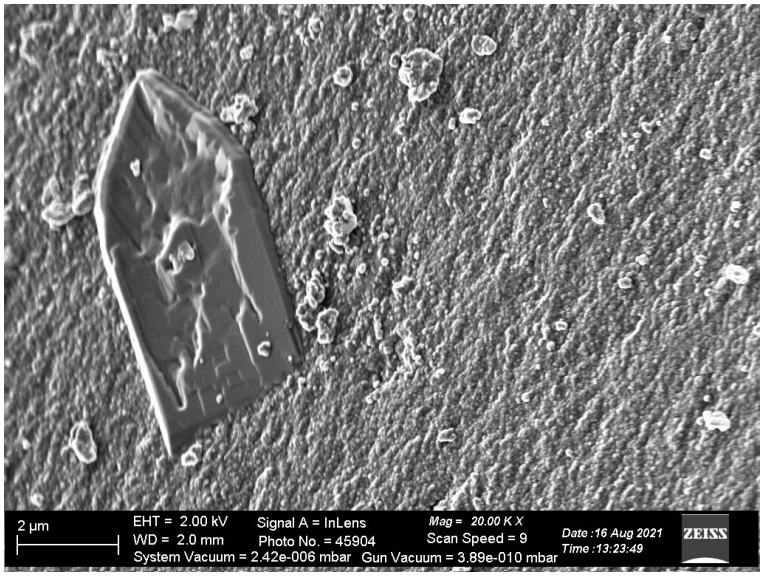

Figure 11: Particle of crystalline, nonporous silica (quartz) formed during support synthesis, embedded in amorphous, mesoporous silica.

4.1.3 Friability tests

Typical catalysts in literature yielded friabilities of less than 1% (Loumi et al., 2022). Friabilities of the catalysts produced in this study are much higher, above 3%, as shown in 12.

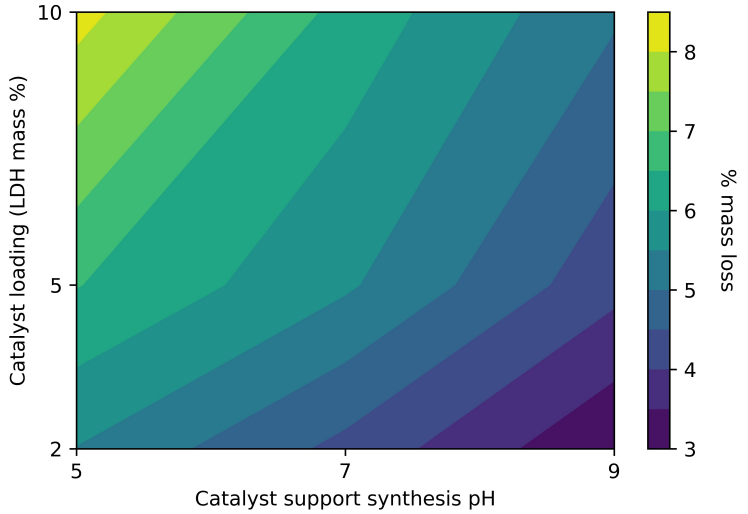

Figure 12: Friability, defined as the % mass loss during friability tests, as a function of catalyst support synthesis pH and LDH loading (mass %).

It was observed that the catalyst friability increases with a decrease in support synthesis pH, and an increase in catalyst loading. The maximum average friability for LDH loadings (mass %) of 2, 5, and 10%, are 5.5%, 6.5%, and 8.2% respectively. Each of these maximums occurred at a support synthesis pH of 5. These maximums indicate a relatively high amount of mass loss and/or catalyst dust formation due to abrasion. This can negatively effect fluidisation processes, resulting in entrainment of fine catalyst dust into the liquid product. If the liquid product is not filtered in the process, catalytic conversion can continue to occur during oil storage as a result of the catalyst dust. The use of binders would remedy this issue, but would likely result in a decrease in surface area. More studies on the effects of adding different binders to the catalyst formulation are required to investigate the trade-off between friability, surface area and pore size.

A higher support synthesis pH of 9 resulted in reduced friabilities of 3.0%, 3.8%, and 5.1% for LDH loadings (mass%) of 2%, 5%, and 10% respectively.

The negative effect of increased LDH loadings on catalyst friability is due to LDH being a friable powder. From these results, it can be deduced that LDH concentrations (mass %) in mesoporous silica-supported catalysts should not exceed 10%. There is little need to increase the concentration beyond this, because the catalyst activity of LDH has been shown to be strong, as will be discussed in the product analysis.

4.2 Exploratory analysis

4.2.1 Elemental analysis

The elemental composition of the dried *E. grandis* sawdust used for pyrolysis was shown to be 45.0% carbon, 5.5% hydrogen, and 49.5% oxygen (by difference). This aligns with other literature, which shows that elemental compositions of various species of Eucalyptus range between 43.8% and 47.1% carbon, 5.6% and 5.9% hydrogen, and 48.1% and 50.6% oxygen (Pereira et al., 2013).

4.2.2 TGA

Figures 13 and 14 show the results of TG analysis of *E. grandis* sawdust with 20% of the various catalyst types, as well as no catalyst and the silica reference catalyst. The pyrolysis

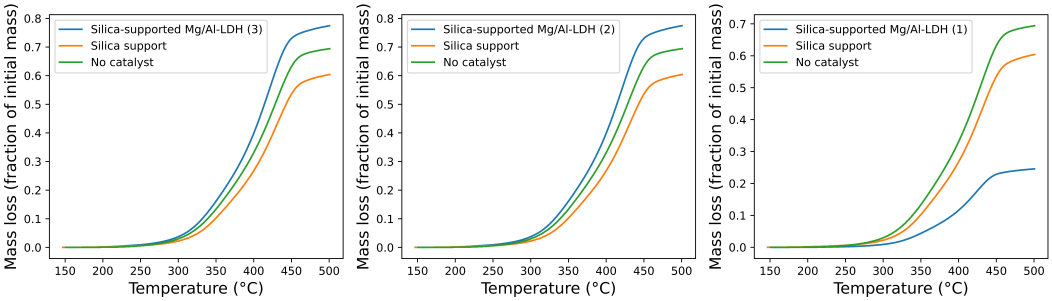

Figure 13: Thermogravimetric results compared between MgAl-LDH catalyst types and support synthesis pHs.

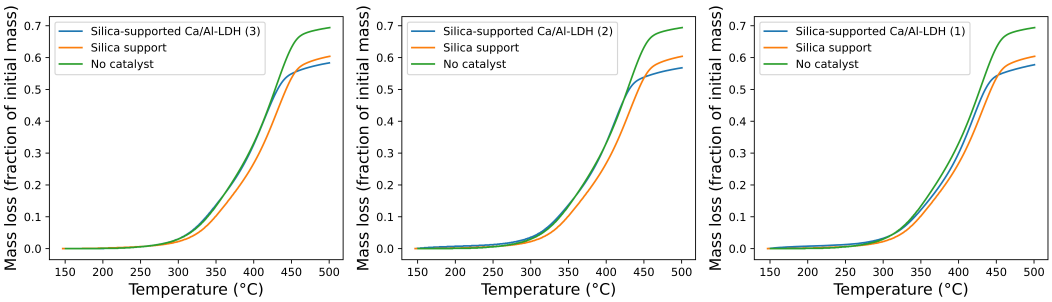

Figure 14: Thermogravimetric results compared between CaAl-LDH catalyst types and support synthesis pHs.

of lignocellulosic biomass in TGA exhibits two distinct heating regions, namely moisture evaporation and removal of volatile compounds below 200 °C, and depolymerisation and decomposition between 200 and 675 °C. The region of maximum mass loss occurs between 300 and 450 °C. This is also the region in which the maximum deviation from the curve with no catalyst can be seen. Overall, there is an almost negligible difference between the curves. There is practically no difference between that of the sample without catalyst, and with reference catalyst. There is a slightly more noticeable difference in the curves of the samples containing CaAl-LDH catalysts, but almost no difference in the curves between the catalyst support synthesis pHs.

These results indicate that the silica support has little influence on the rate of the overall reaction, at simulated fast pyrolysis conditions. CaAl-LDH appears to result in a higher amount of the biomass being converted to gas, which is likely as a result of increased decarboxylation reactions. The same effect was observed with the MgAl-LDH, but to a lesser extent. The final MgAl-LDH catalyst (with the largest pore diameter and smallest surface area), in particular, resulted in a much lower conversion. This is possible as a result of more conversion of larger molecules, and less conversion of smaller molecules.

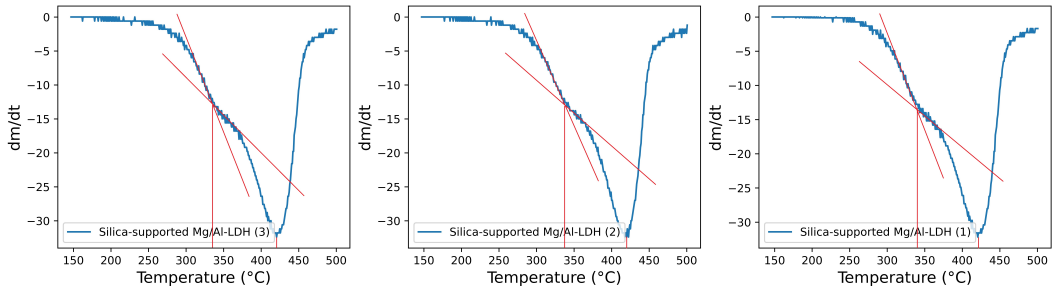

Figure 15: Differential TG results compared between MgAl-LDH catalyst types and support synthesis pHs. Inflection points are indicated by the crossing red gradient lines.

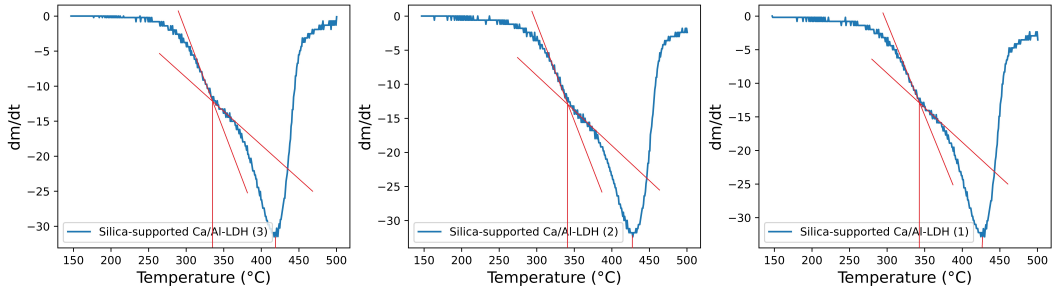

Figure 16: Differential TG results compared between CaAl-LDH catalyst types and support synthesis pHs. Inflection points are indicated by the crossing red gradient lines.

Figures 15 and 16 represent the differential TG curves for the catalysts. There is almost no difference in the inflection points pertaining to peak hemicellulose degradation (around 350 °C) and peak cellulose degradation (around 450 °C). The lack of catalyst activity observed during TG analysis, in particular the differential TG analysis, may be as a result of the fact that this is essentially a batch reaction occuring at a slower heating rate.

4.3 Pyrolysis oil characteristics

4.3.1 Product yields

Figure 17 shows the change in oil, gas and char yields, as well as the change in heat exchanger and ESP oil yields, with the use of the different catalysts. The average total oil yield of runs without catalyst was 37.6%, while that of runs with the catalyst support was 35.5%. This is consistent with other studies at similar reaction conditions, which yielded around 36.0% oil (Heidari et al., 2014). The higher gas yields are as a result of operating the reactor at 600 °C. The total oil yields for MgAl-LDH catalysts were 32.9, 36.9 and 38.6% for a support synthesis pHs of 5, 7 and 9 respectively. CaAl-LDH catalysts produced higher total oil

yields of 37.5, 43.7 and 47.2% for the respective support synthesis pHs. The same trend was observed for the fractions of ESP oil that make up the total oil yields, with ESP oil portions of 25.7, 30.3 and 35.8% for increasing catalyst synthesis pHs. The increase in yields for each type of LDH correspond to decreasing BET surface areas and increasing BJH average pore widths.

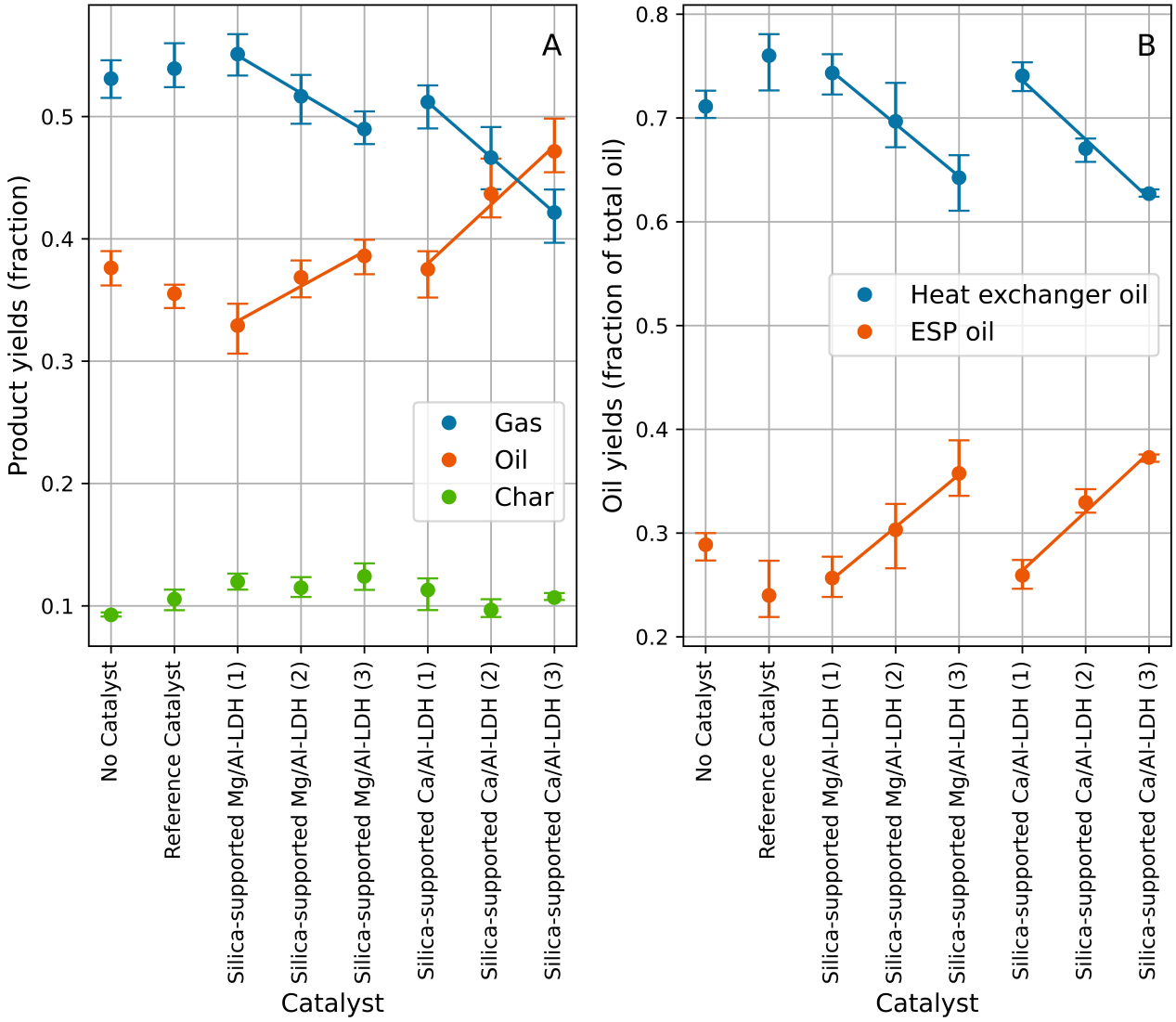

Figure 17: (A) represents the change in oil, gas and char fractions with change in catalyst, and (B) represents the change in heat exchanger (HE) oil and electrostatic precipitator (ESP) oil fractions of the total oil product with change in catalyst.

The increase in heat exchanger oil yields for each catalyst appears to correspond to decreasing catalyst surface areas, and increasing pore sizes (which in turn corresponds to increasing catalyst synthesis pH). A possible explanation for this is that larger pore sizes produce larger

molecules due to the active sites being occupied by larger molecules that were able to enter the catalyst support matrix. The heat exchanger oils would contain these larger molecules, as they would be the molecules that would condense first at higher temperatures (around 70 °C). For example, the heat exchanger oils contain a relatively large amount of methanol as evidenced by the GC/MS results, which are discussed in subsequent sections. Although this is not a large molecule, it has a relatively high boiling point (around 65 °C), and would thus be condensed primarily in the heat exchanger, similar to water. Therefore, larger pore sizes would correspond to an increased primary heat exchanger/condenser oil yield. It would then make sense that smaller catalyst pore sizes would produce larger quantities of ESP oil, as the ESP condenses the smaller molecules that are more difficult to condense. This is the trend that is observed in this set of results.

One can gather from these clear trends that the catalysts are efficient. The functionality of a catalyst with a high number of active sites (as indicated by the relatively high catalyst surface areas) would be more significantly affected by the difference in pore diameters, than a catalyst with sparse active sites.

The quantities of oil collected in the ESP are lower than expected when considering literature values under similar conditions (around the 50% of the total oil collected (Moutsoglou et al., 2018)). However, this low value is likely attributed to the large quantity of water found in the oils, as discussed in following sections. This water is collected primarily in the condenser.

4.3.2 Functional group analysis

The most notable differences in the FTIR spectra, as shown in Figure 18, are in the large peak, around 3200 cm^{-1}. The broad peak around this wavenumber indicates the presence of -OH groups that are linked to alcohols, carboxylic acids, and water.

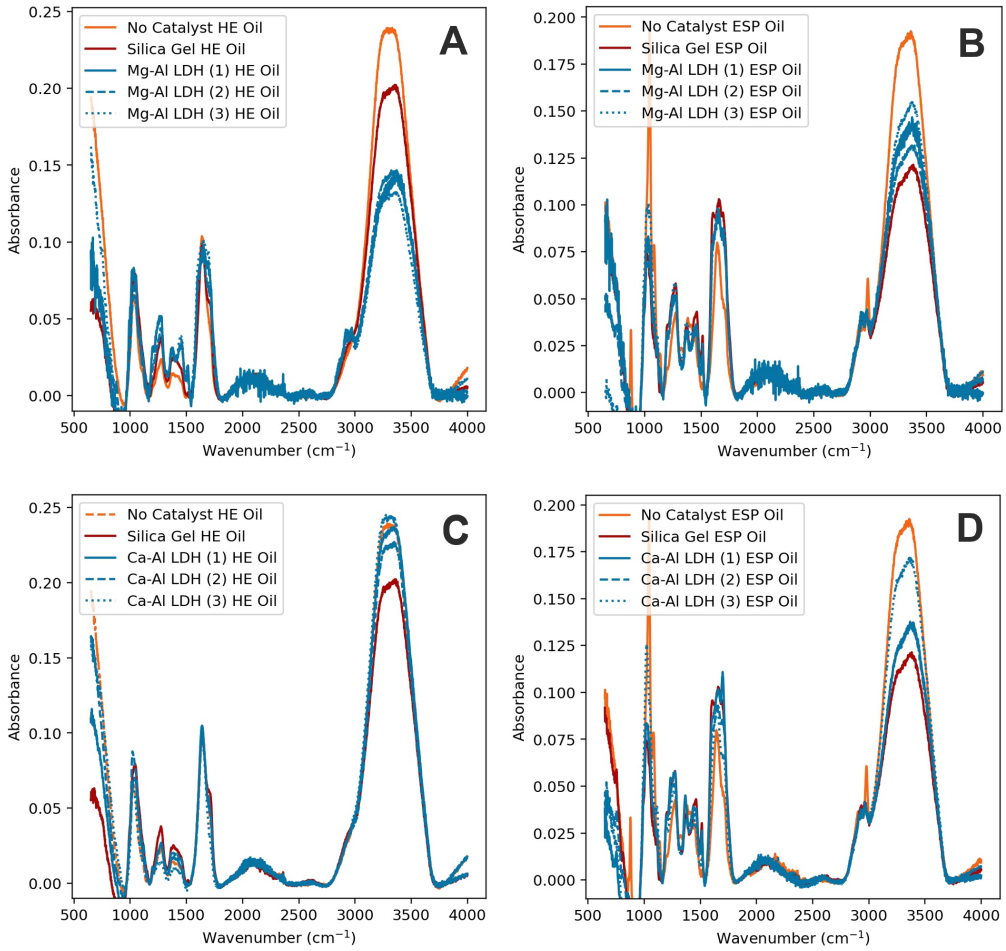

Figure 18: FTIR spectra of (A) the Mg-Al LDH doped catalysts heat exchanger oils and (B) ESP oils, and (C) the Ca-Al LDH doped catalysts heat exchanger oils and (D) ESP oils.

-OH groups that are linked to phenols are shown by the broad peak around 3000 cm^{-1}. With the second largest peak around 1600 cm^{-1}, the dominance of these peaks are likely to be attributed to high water contents. There is a noticeable decrease in the peak around 3200 cm^{-1} with the catalyst support alone compared to no catalyst, for both the heat exchanger and ESP oils. For the heat exchanger oils, the decrease is even more prominent for all three Mg-Al LDH catalysts, where the opposite effect is seen for the CaAl-LDH catalysts.

For the ESP oils, the 3200 cm^{-1} peak of the MgAl-LDH catalyzed oils, corresponding to alcohols, carboxylic acid and water, lies between that of the catalyst support and no catalyst. The same is observed for the CaAl-LDH catalyzed oils, but the peaks are larger.

These results indicate that the catalyst support itself contributes to a significantly lower

concentration of -OH stretching vibrations, likely to be indicative of water, but also partly because of carboxylic acids, alcohols and phenolic groups. This trend is evident in both the heat exchanger and ESP oils. Oils catalyzed by MgAl-LDH further decreased these levels in the heat exchanger oils, but not the ESP oils. Oils catalyzed by CaAl-LDH increased the concentration of -OH stretching vibrations in both the heat exchanger and ESP oils. For all three catalyst support synthesis pHs of each LDH catalyst, the results were similar.

Other changes in the heat exchanger oil FTIR spectra included an increase in the peak around 1450 cm^{-1}, indicating carbon double-bond stretching such as those present in aromatic rings, as a result of the silica support. Doping of the support with MgAl-LDH increased this peak, while CaAl-LDH decreased this peak. The same effect was observed for the peak around 1250 cm^{-1}, indicating alkane deformation. In the ESP oils, the catalyst support and MgAl-LDH catalysts resulted in a decrease in the peak around 1050 cm^{-1}, indicating ethers and alcohols. This peak increased in size with the CaAl-LDH catalysts.

While there were noticeable differences in the peaks produced with LDH-catalyzed oils, there was very little difference in the same LDHs, with supports catalyzed at different pHs. This indicates that surface areas and average pore widths do not play a significant role in the sizes of -OH stretching peaks.

4.3.3 Water content determination

The Python code for FTIR peak deconvolution and water content determination are shown in Appendix C. Figure 19 shows the deconvolution of the FTIR peaks that were used to determine water content in the heat exchanger oils produced without catalyst, and with silica catalyst. The bond vibrations corresponding to the deconvoluted peaks were identified according to the Table 3.

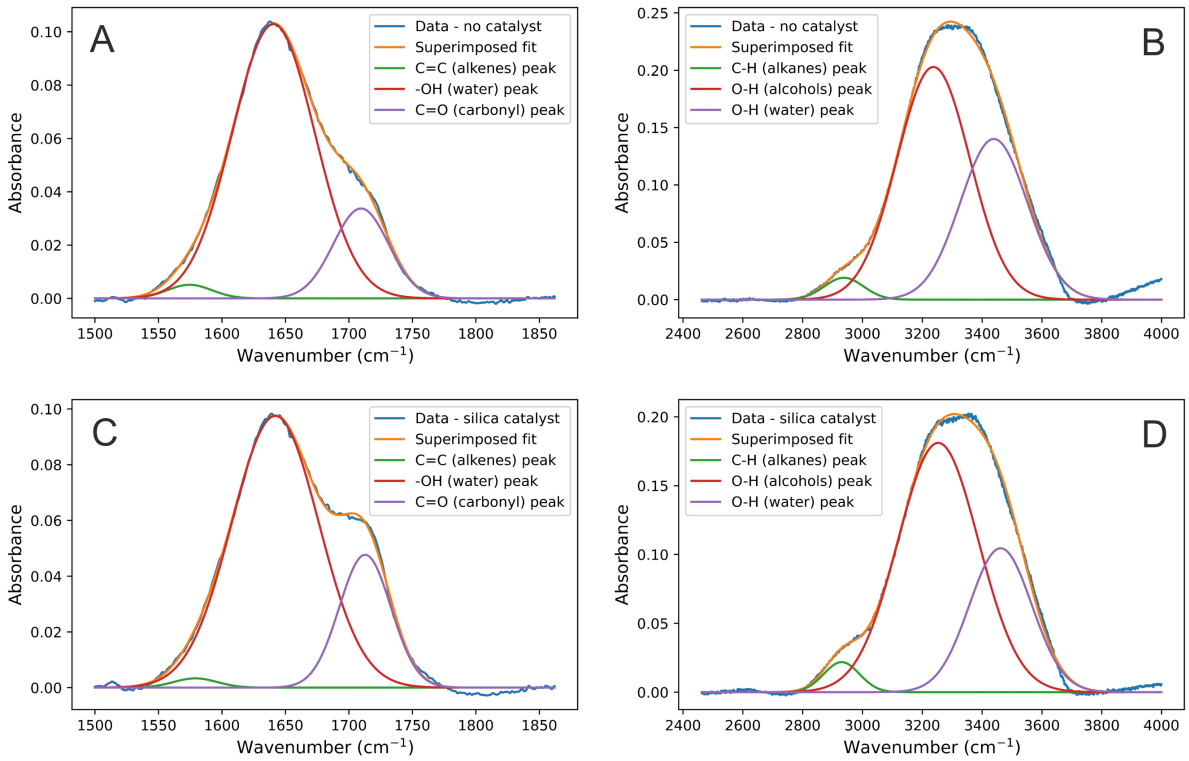

Figure 19: Deconvolution of FTIR 1650 cm^{-1} and 3400 cm^{-1} peaks of heat exchanger oils produced without catalyst, and with silica catalyst support. (A) shows the peaks around 1650 cm^{-1} for heat exchanger oils without catalyst, and (B) the peaks around 3400 cm^{-1}. (C) shows the peaks around 1650 cm^{-1} for heat exchanger oils with silica catalyst support, and (D) the peaks around 3400 cm^{-1}.

FTIR water analysis of silica-catalysed heat exchanger oils The first notable difference is the slight decrease in water content with the use of the silica catalyst support, mainly visible around the 3400 cm^{-1} peak. There is also evidence of an increase in carbonyl groups and alkane bonds.

FTIR water analysis of MgAl-LDH-catalysed heat exchanger oils A large difference can be seen in Figure 20, particularly in the 1650 cm^{-1} peak. This indicates a significant decrease in the water content of the heat exchanger oils produced with the MgAl-LDH catalysts. In addition, the 1650 cm^{-1} water peak decreased from around 0.08 to around 0.04, with an increase in catalyst support synthesis pH from 5 to 9. There is no significant difference in the sizes of the 3400 cm^{-1} water peaks between the catalyst support synthesis pHs for the MgAl-LDH catalysts. However, this peak is smaller for the heat exchanger oils produced

with MgAl-LDH catalysts than for those produced with no catalyst, or with the silica catalyst support. In addition to the water peaks, there was a large increase in the alkenes peak for the MgAl-LDH catalysts, and this peak continued to increase with increasing catalyst support synthesis pH.

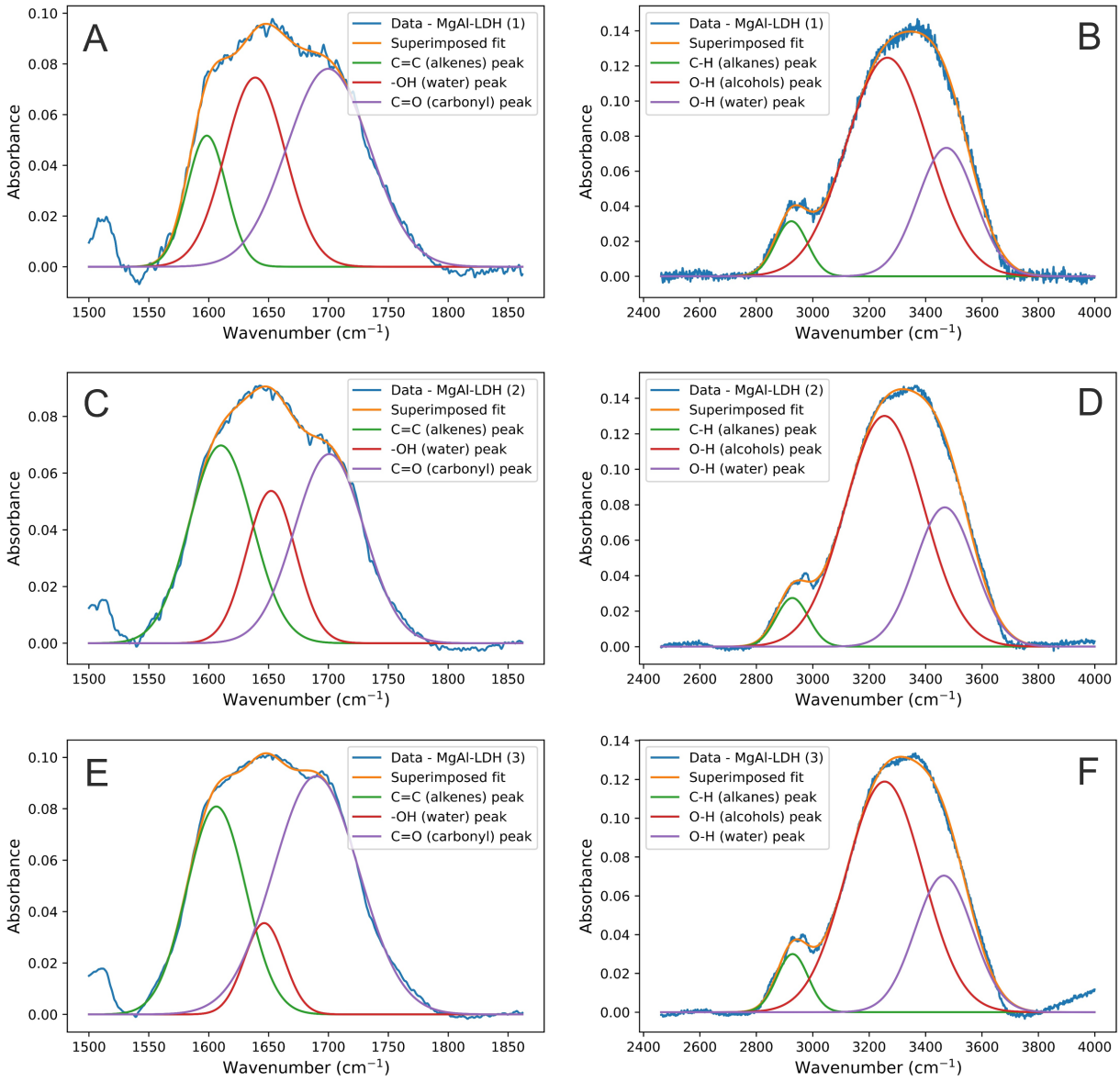

Figure 20: Deconvolution of FTIR 1650 cm^{-1} and 3400 cm^{-1} peaks of heat exchanger oils produced with MgAl-LDH catalysts. (A) shows the peaks around 1650 cm^{-1} for heat exchanger oils with MgAl-LDH catalyst 1, and (B) the peaks around 3400 cm^{-1}. (C) shows the peaks around 1650 cm^{-1} for heat exchanger oils with MgAl-LDH catalyst 2, and (D) the peaks around 3400 cm^{-1}. (E) shows the peaks around 1650 cm^{-1} for heat exchanger oils with MgAl-LDH catalyst 3, and (F) the peaks around 3400 cm^{-1}.

FTIR water analysis of CaAl-LDH-catalysed heat exchanger oils Figure 21 shows that the water peaks of the heat exchanger oils produced with CaAl-LDH catalysts are similar in size to those produced without catalyst. Neither do there appear to be any significant difference between the different catalyst support synthesis pHs. There also does not appear to be any significant differences in the carbonyl, alkenes or alkanes peaks. This is evidence that the catalytic activity of CaAl-LDH catalysts, particularly towards the heavier compounds found in the heat exchanger oils, is similar to that of the silica support.

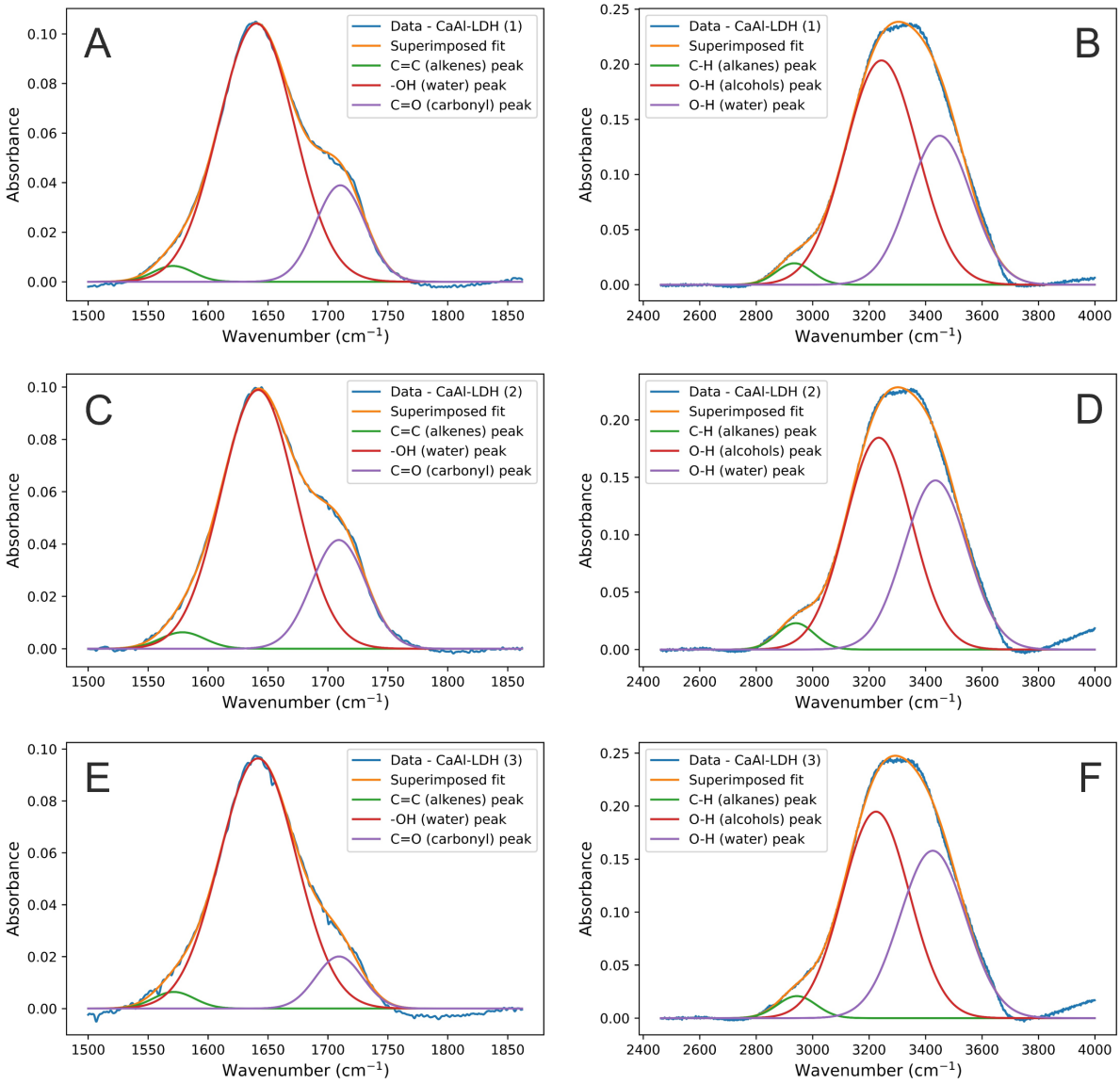

Figure 21: Deconvolution of FTIR 1650 cm^{-1} and 3400 cm^{-1} peaks of heat exchanger oils produced with CaAl-LDH catalysts. (A) shows the peaks around 1650 cm^{-1} for heat exchanger oils with CaAl-LDH catalyst 1, and (B) the peaks around 3400 cm^{-1}. (C) shows the peaks around 1650 cm^{-1} for heat exchanger oils with CaAl-LDH catalyst 2, and (D) the peaks around 3400 cm^{-1}. (E) shows the peaks around 1650 cm^{-1} for heat exchanger oils with CaAl-LDH catalyst 3, and (F) the peaks around 3400 cm^{-1}.

FTIR water analysis of silica-catalysed ESP oils The catalytic activity of the silica support is more evident in Figure 22, as seen by the increases in the alkene and carbonyl peaks. In general, the water content of the ESP oils is less than the heat exchanger oils. This

is likely because the greater volume of the water is condensed in the heat exchanger, before the pyrolysis gases reach the ESP. Like the heat exchanger oils, there is little difference in the sizes of the water peaks between the ESP oils produced without catalyst, and with silica support. In addition, the alkane peaks are much larger in the ESP oils. This indicates a much higher concentration of aliphatic chains.

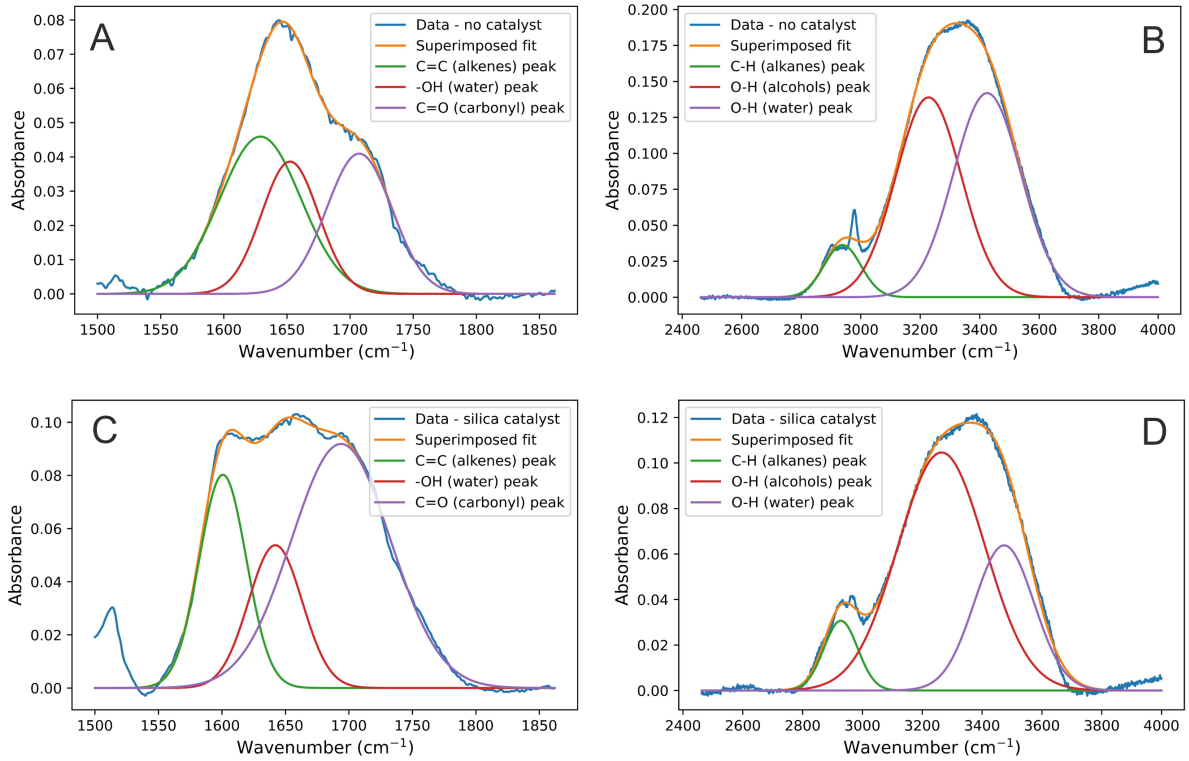

Figure 22: Deconvolution of FTIR 1650 cm^{-1} and 3400 cm^{-1} peaks of ESP oils produced without catalyst, and with silica catalyst support. (A) shows the peaks around 1650 cm^{-1} for ESP oils without catalyst, and (B) the peaks around 3400 cm^{-1}. (C) shows the peaks around 1650 cm^{-1} for ESP oils with silica catalyst support, and (D) the peaks around 3400 cm^{-1}.

FTIR water analysis of MgAl-LDH-catalysed ESP oils Unlike the heat exchanger FTIR spectra, it appeared as though there was a small increase in the water peaks of the ESP oils produced with MgAl-LDH catalysts. This can be seen in Figure 23. The sizes and ratios of the peaks of the ESP oils produced with MgAl-LDH catalyst are similar to those produced with silica catalysts. There is also very little difference between the sizes of the water peaks for the different catalyst support synthesis pHs.

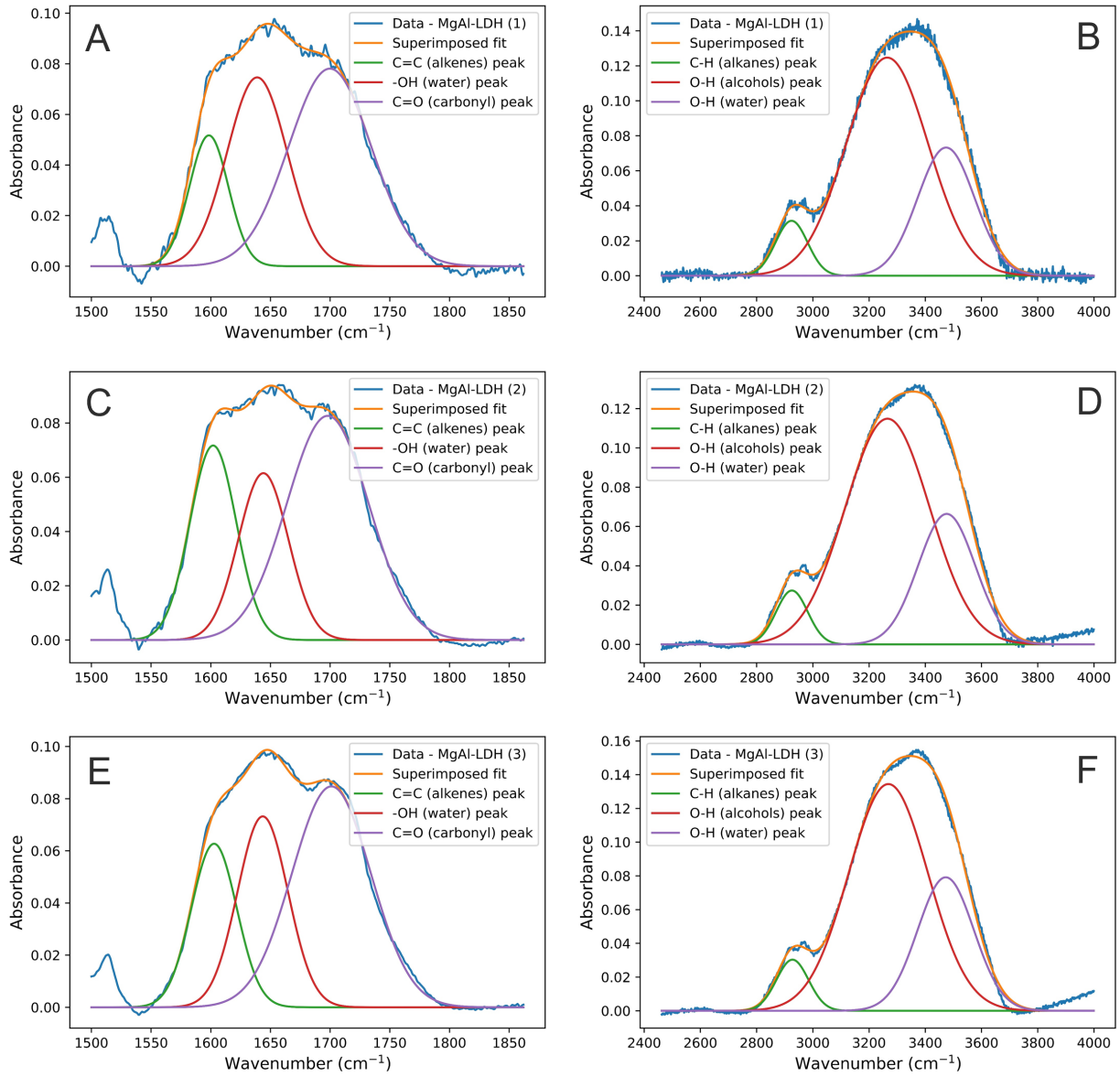

Figure 23: Deconvolution of FTIR 1650 cm^{-1} and 3400 cm^{-1} peaks of ESP oils produced with MgAl-LDH catalysts. (A) shows the peaks around 1650 cm^{-1} for ESP oils with MgAl-LDH catalyst 1, and (B) the peaks around 3400 cm^{-1}. (C) shows the peaks around 1650 cm^{-1} for ESP oils with MgAl-LDH catalyst 2, and (D) the peaks around 3400 cm^{-1}. (E) shows the peaks around 1650 cm^{-1} for ESP oils with MgAl-LDH catalyst 3, and (F) the peaks around 3400 cm^{-1}.

FTIR water analysis of CaAl-LDH-catalysed ESP oils Figure 24 shows an increase in the ESP oil water content with the use of CaAl-LDH catalysts. There is also a small increase in the carbonyl peaks. As can be seen in (A), the sizes of the respective peaks change the overall shape of the combined peak. The sizes of the water peaks appear to

change with the different catalyst support synthesis pHs, but there does not appear to be any notable correlation.

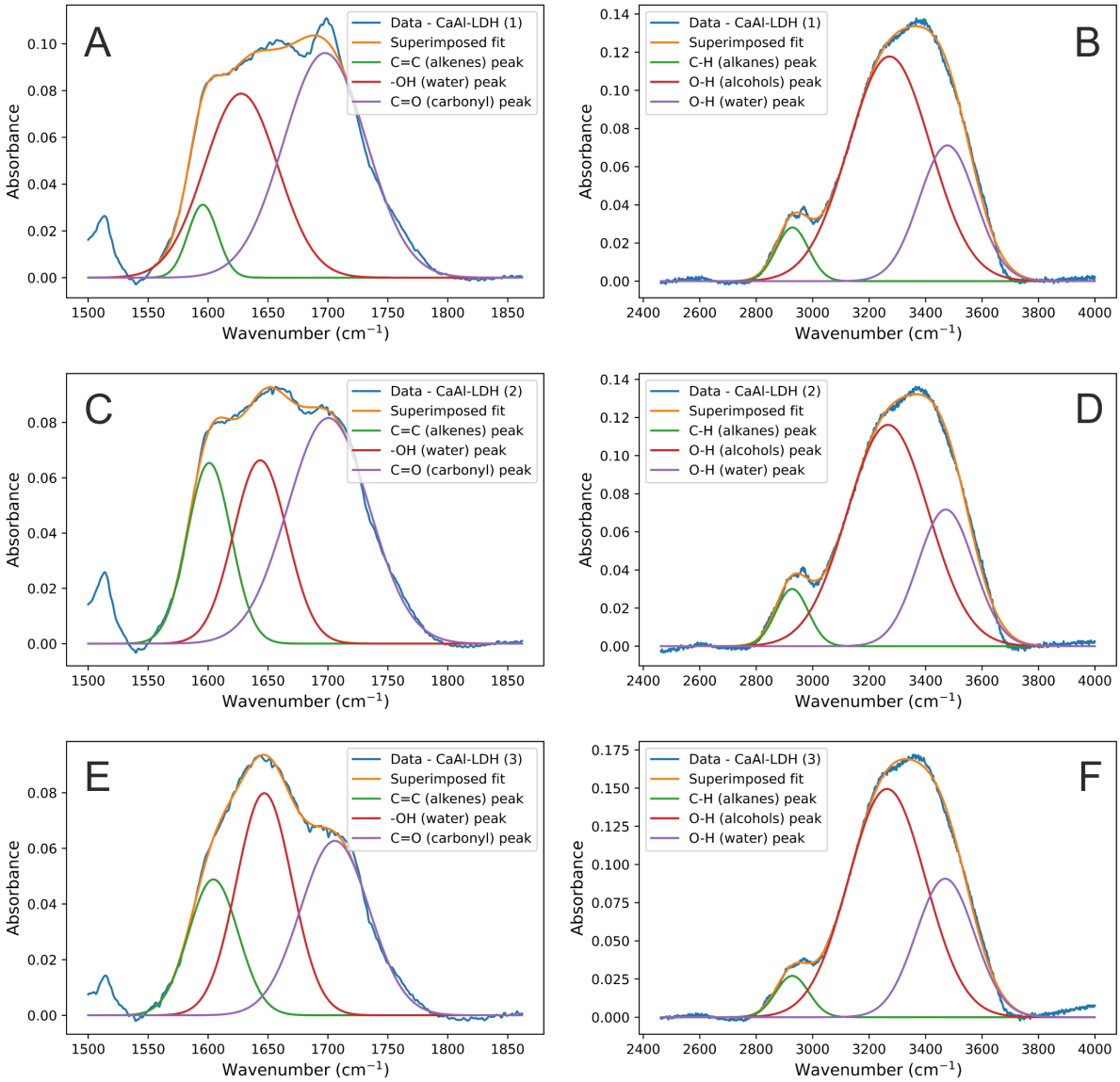

Figure 24: Deconvolution of FTIR 1650 cm^{-1} and 3400 cm^{-1} peaks of ESP oils produced with CaAl-LDH catalysts. (A) shows the peaks around 1650 cm^{-1} for ESP oils with CaAl-LDH catalyst 1, and (B) the peaks around 3400 cm^{-1}. (C) shows the peaks around 1650 cm^{-1} for ESP oils with CaAl-LDH catalyst 2, and (D) the peaks around 3400 cm^{-1}. (E) shows the peaks around 1650 cm^{-1} for ESP oils with CaAl-LDH catalyst 3, and (F) the peaks around 3400 cm^{-1}.

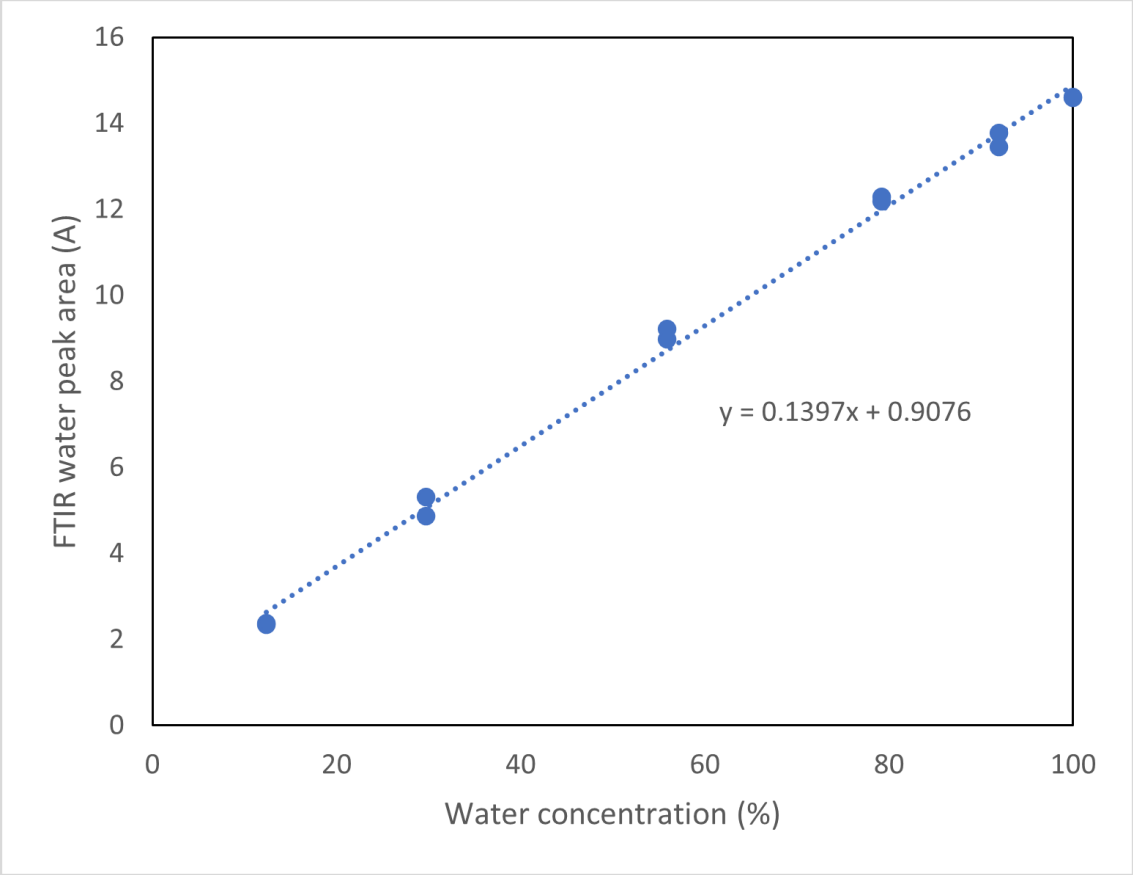

Figure 25: Fitted calibration curve of FTIR 1600 cm^{-1} water peak at different concentrations of water in ethanol, used in the determination of pyrolysis oil water contents.

Water content calibration fitting via FTIR Figure 25 shows the water calibration curve produced by analysis of the 1600 cm^{-1} and 3400 cm^{-1} peaks of water-ethanol solutions with varying concentrations. For the purpose of the mass % calculation, the volume % were converted to mass %. The curve was used to determine the water content of the heat exchanger and ESP oils, according to their water peak area. The peak used for this calculation was the 1600 cm^{-1} water peak, because in a mixture of ethanol and water, the peak formed around this wavenumber does not need to be deconvoluted, as there are no overlapping peaks. Table 4 shows the results of these interpolations.

Pyrolysis oil water content determination Typically, water contents of fast pyrolysis oils are in the range of 15% and 30% (Carrier et al., 2014). The high water contents achieved in the experiments are likely attributed to process inefficiencies. A redesign and reconfiguration of the reactor system, including an initial condensation step primarily intended to

Table 4: Results of FTIR water content determination in fast pyrolysis oils

Catalyst	HE oil 1600 cm^{-1} water peak area	ESP oil 1600 cm^{-1} water peak area	HE oil water content (mass %)	ESP oil water content (mass %)
No catalyst	14.22	4.37	95.29	24.77
Silica	14.26	5.69	95.59	34.26
MgAl-LDH (1)	9.40	9.40	60.78	60.78
MgAl-LDH (2)	5.50	6.44	32.89	39.62
MgAl-LDH (3)	2.97	7.75	14.76	48.96
CaAl-LDH (1)	14.04	12.07	94.02	79.91
CaAl-LDH (2)	12.85	7.43	85.48	46.67
CaAl-LDH (3)	13.00	9.25	86.53	59.74

remove water, should be considered in future studies. Both the heat exchanger and ESP oils contained a single liquid phase. These were aqueous in the case of the heat exchanger oils, and organic in the case of the ESP oils. The heat exchanger oils contained much more water, on average, than the ESP oils. This shows why the heat exchanger oils could not be used for bomb calorimetry measurements, and why traditional water content determination methods such as Karl Fischer titration could not be used. Distilling both the heat exchanger and ESP oils may enable the use of these methods.

The overall observation is that the MgAl-LDH catalysts produced heat exchanger oils with significantly less water (up to 85 % less). In other literature, MgAl-LDH is also shown to decrease water by more than 65%. This is likely as a result of dehydration, decarbonylation and decarboxylation reactions catalysed by MgAl-LDH (Mysore Prabhakara et al., 2022). The CaAl-LDH catalysts also appeared to decrease the heat exchanger oil water content slightly. However, the ESP oil water content was higher with the use of the catalysts, including the silica catalyst support alone. There was a significant increase in the ESP oil water content as a result of all three CaAl-LDH catalysts. For both the MgAl- and CaAl-LDH catalysts, the catalyst with support synthesised at a pH of 5 appeared to increase the heat exchanger and ESP oil water content to the greatest extent. This is likely to do with the smaller pore size. Therefore, smaller molecules were more readily converted to water and other light molecules, whereas larger pore sizes created more competition for active sites, resulting in less water formation.

4.3.4 Chemical composition analysis

The expanded GC/MS results (peak area % for each detected compound) are presented in Appendix B. The effect of the reference catalyst (mesoporous silica support) on the compositions of the heat exchanger oil organic fractions and ESP oils in comparison to the uncatalyzed oils showed that there was a small amount of catalytic activity in the catalyst support alone. This is shown in 26.

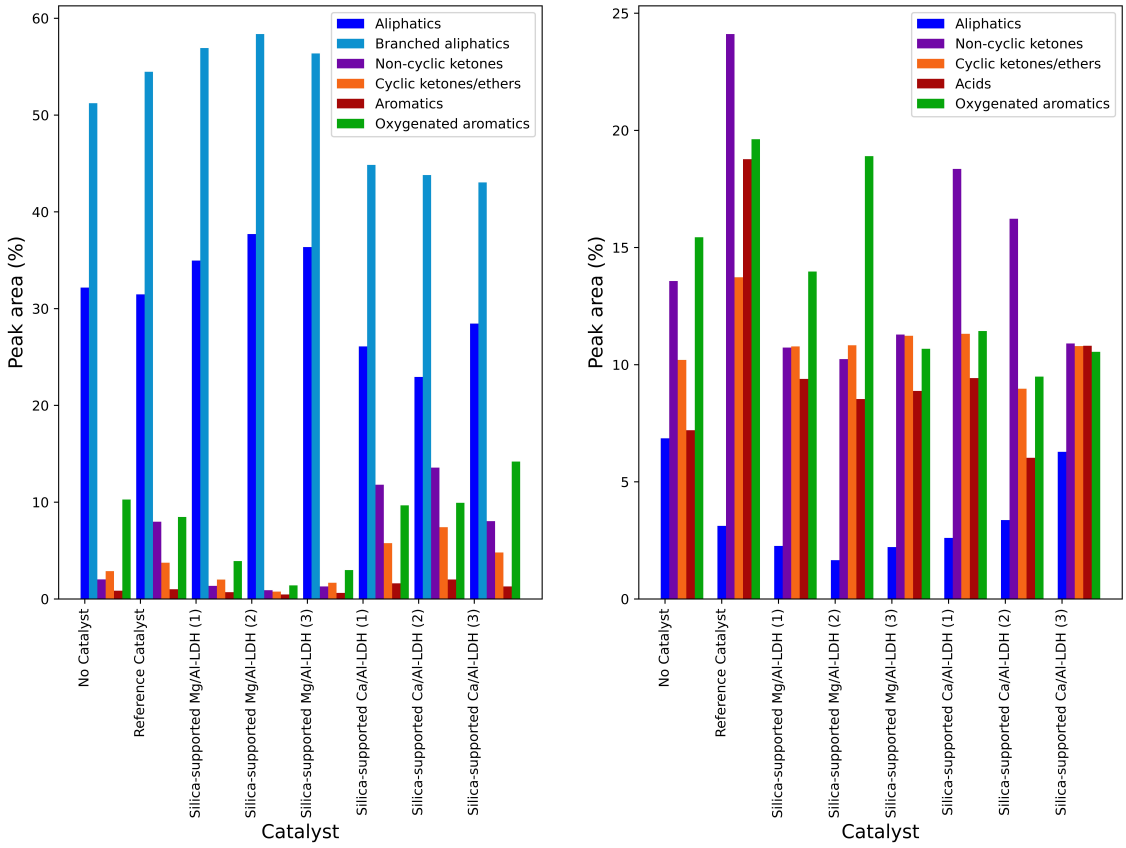

Figure 26: GC analysis of (A) ESP oils and (B) HE oils produced by fast pyrolysis of *E. grandis* sawdust using different catalysts.

The heat exchanger oil organic fraction compositions in peak area percents showed a decrease in aliphatics from 6.9% to 3.1% with the use of the reference catalyst. There was a rise in oxygenates, such as non-cyclic ketones, aldehydes and esters including methyl glyoxal, isopropyl acetate and succinaldehyde, from 13.0% to 24.1%. Carboxylic acids such as acetic and octanoic acids also rose from 7.2% to 18.8%. Compositions are similar to those reported for model fast pyrolysis compounds such as acetic acid, furfural, catechol, and 4-methyl-1,2-benzendiol (3.3%, 3.4%, 1.9% and 0.7%) (Merckel, 2014). The ESP oil

compositions of aliphatics such as hexane and heptane, cyclic ethers and ketones such as furfural, 3-furaldehyde, butyrolactone and benzaldehyde, and non-oxygenated aromatics such as toluene, xylene and naphthalene were similar (31.5%, 3.7% and 1.0% respectively). However, the support resulted in a small increase in branched aliphatics such as methyl-pentane and methyl-hexane (51.2% to 54.5%), a small decrease in oxygenated aromatics such as phenol, methyl-, dimethyl- and trimethyl-phenol (10.3% to 8.5%), and a more notable increase in non-cyclic ketones such as acetone and hydrazinecarboxamide (2% to 8%). These small catalytic effects are likely as a result of the slightly acidic properties of exposed silanol groups present in the support. The overall effect of the silica support alone on the quantity of oxygenated compounds is very small. However, the silica support appears to favour the formation of heavier oxygenates, as evidenced by the larger proportion of oxygenates in the heat exchanger oil fractions.

Influence of MgAl-LDH on GC/MS results MgAl-LDH catalysts resulted in lower oxygenate compositions in the heat exchanger organic fractions compared to the reference catalyst, with a composition similar to that of the non-catalyzed heat exchanger oils. The changes in compositions of the ESP oils are more apparent. The most notable change is the decrease in ketones, ethers, non-oxygenated and oxygenated aromatics throughout all three catalyst support synthesis pHs. There was very little change in the compositions of the heat exchanger organic fractions throughout all three MgAl-LDH catalysts, except for an increase (to 18.9%) in oxygenated aromatics in catalyst 2. All three MgAl-LDH catalysts also displayed an increase in aliphatics and branched aliphatics in the ESP oils. The catalyst synthesized at a pH of 7 appears to have the lowest amount of oxygenates (3.1%) and aromatics (0.5%), as well as the highest amount of aliphatics (96.1%). Oils for MgAl-LDH catalysts synthesized at pHs of 5 and 9 contain almost identical compositions (91.9%, 3.4%, 3.9%, and 0.7% for aliphatics, ketones and ethers, oxygenated aromatics and non-oxygenated aromatics respectively). All three MgAl-LDH catalysts yielded acid contents of between 5-10% similar to those reported in literature for the same catalyst and similar operating conditions (Mysore Prabhakara et al., 2022). However, ketones content were significantly less in this study (above 30.0% in the other study). The results for the MgAl-LDH catalysts show that the catalyst support synthesis pH, and thus the catalyst pore width, plays a small role in the compositions of the oils produced. MgAl-LDH supported by mesoporous silica with an intermediate pore size of around 4 nm produces more heavy oxygenated aromatics and more light aromatics.

Influence of CaAl-LDH on GC/MS results CaAl-LDH catalysts had the opposite effect on the ESP oils to the MgAl-LDH catalysts. The concentrations of aliphatics and branched aliphatics decreased (26.1% and 44.9% respectively) while the concentrations of oxygenates and aromatics increased (27.2% and 1.6% respectively). The increase in oxygenates as a result of CaAl-LDH compared to MgAl-LDH is likely as a result of the differences in acid-base properties between the two catalysts. CaAl-LDH contains stronger basic sites than MgAl-LDH (Arrabito et al., 2019). An increased effect was also observed in the CaAl-LDH catalyst synthesized at a pH of 7, similar but opposite to the effect noticed in the Mg-Al LDH catalyst. With the exception of higher non-cyclic ketones, aldehydes and esters compositions (above 15.0%), the compositions of heat exchanger oil organic fractions did not vary significantly with the use of CaAl-LDH catalysts. This indicates that CaAl-LDH catalysts results in little change to the heavier fraction, but notable change to the lighter fraction.

GC/MS results in relation to catalyst pore size With the low organic fractions in the heat exchanger oils as a result of high water content, as well as the lack of useful GC/MS data for these fractions, there is not enough evidence from analysis of the heat exchanger oils to confirm catalytic activity. However, similar trends in the MgAl- and CaAl- LDHs, synthesis pHs and ESP oil compositions suggest that a catalyst support synthesis pH of 7 has the highest catalytic activity. A synthesis pH of 7 correlates to an intermediate BET surface area and pore size of around 520 m^2/g and 4 nm respectively. The pronounced difference in the compositions of the ESP oils with the different catalysts, as well as the small difference in the composition of the heat exchanger oil fractions, suggests that the current catalyst pore size range is better suited for improving the lighter pyrolysis oil fractions as opposed to the heavier fractions. Larger pore sizes should be investigated to assess differences in the heavier fractions.

Taking into account the small amount of catalytic activity in the support itself, it is evident that MgAl-LDH has shown to have the greatest oxygen removal efficiency, and a mesoporous silica catalyst support synthesis pH of 7 yields the most favourable result. CaAl-DH has shown to have the lowest oxygen removal efficiency. In fact, CaAl-LDH may even be responsible for increasing the ESP oil oxygen content in comparison to the ESP oil produced without catalyst.

4.3.5 GC/MS results compared to FTIR results

The primary findings of the FTIR results (and the functional groups in particular) were that the -OH band around 3200 cm^{-1}, corresponding to carboxylic acids and alcohols, were drastically less for MgAl-LDH catalysed heat exchanger oils than that of silica or no catalyst. CaAl-LDH had very little effect on this band. The same finding was made for the ESP oils, but to a lesser extent. Interestingly, for the heat exchanger oils, this trend is not clear in the GC/MS results. This is likely as a result of the high water content, which makes the changes concentrations of other compounds appear to be less noticeable.

However, for the ESP oils, there is a marked decrease in the concentration of oxygenated aromatics (such as phenols) and non-cyclic ketones which may belong to carboxylic acid groups, when catalysed by MgAl-LDH. This is also evident in the FTIR band around 3000 cm^{-1}.

4.3.6 Bomb calorimetry

Dried *E. grandis* biomass was found to have an average HHV of 15.9 ±3.9 MJ/kg. The HHV of the pyrolysis ESP oils without the use of a catalyst improved slightly to 16.2 ±2.2 MJ/kg on a wet basis without ash removal, and the reference catalyst produced ESP oils with a higher HHV of 19.6 ±1.9 MJ/kg.

Use of the Mg-Al LDH catalysts yielded improved ESP oil HHVs of 21.7 ±0.9 MJ/kg, 21.3 ± 2.6 MJ/kg and 22.5 ±1.0 MJ/kg respectively. The increases may be as a result of larger aliphatics concentrations in the Mg-Al LDH catalyzed ESP oils. However, there was no significant difference in the HHV values between the three mesoporous silica supports, likely as a result of the similar compositions.

All three Ca-Al LDH catalysts also produced lower ESP oil HHVs of 17.0 ±2.5 MJ/kg, 15.7 ±0.8 MJ/kg and 15.0 ±0.4 MJ/kg respectively. The lower HHVs are likely due to the higher oxygenates concentrations and higher FTIR -OH peaks.

Table 5 displays the bomb calorimetry results, including the yielded output MJ per kg dry biomass.

The HHV values achieved for the *E. grandis* fast pyrolysis oils are lower than those reported for similar feedstocks at similar reaction conditions (24.5 MJ/kg) (Ben et al., 2019) (Anoop

Table 5: Bomb calorimetry results

Catalyst	ESP oil MJ/kg	Overall yield MJ/kg biomass
No catalyst	16.2	1,8
Silica catalyst	19.6	1.7
MgAl-LDH (1)	21.7	1.8
MgAl-LDH (2)	21.3	2.4
MgAl-LDH (3)	22.5	3.1
CaAl-LDH (1)	17.0	1.7
CaAl-LDH (2)	15.7	2.3
CaAl-LDH (3)	15.0	2.6

et al., 2014) (Chen, Zhang, Xiao, Sun and Song, 2020). This is likely as a result of inefficiencies in the reactor system used in the investigation, resulting in a higher water content. The HHVs of pyrolysis oils can be improved using an optimized system, and are expected to be higher as a result of MgAl-LDH catalysts.

5 Conclusion and recommendations

Biomass fast pyrolysis oil is being investigated as an alternative to fossil fuels because it is renewable and the combustion thereof produces less greenhouse gas emissions. Fast pyrolysis of *E. grandis* in a tail-gas recirculating spouted bed reactor system gives good pyro-oil yields, but the oils are unstable, corrosive and have low higher heating values as a result of high water and oxygen contents. This study investigated the use of mesoporous silica-supported layered double hydroxide catalysts to decrease the oxygen contents in pyro-oils produced in the fast pyrolysis of *E. grandis* sawdust in the aforementioned system.

The catalysts yielded promising results, with high surface areas and high activities (especially MgAl-LDH). However, the friabilities of the catalyst supports, upon exposure to fluidisation abrasion, were high. It is recommended that studies are conducted around the addition of binder chemicals to the catalyst formulation, to investigate the trade-off between improved hardness and loss of surface area, or pore size controllability.

FTIR analysis of the heat exchanger and electrostatic precipitator (ESP) oils showed that the pyrolysis oil generated in the presence of the MgAl-LDh catalysts showed a reduced

intensity for the OH absorption bands, and CaAl-LDH catalysts had little influence on these peaks. GC/MS results of the ESP and heat exchanger oils showed that the MgAl-LDH catalyst supported by mesoporous silica synthesized at a pH of 7 produced an ESP oil with the lowest oxygenates concentration, while the Ca-Al LDH catalyst with a silica gel support synthesized at a pH of 7 yielded the greatest increase in the oxygen contents of ESP oils. The composition of the organic fraction of the heat exchanger oils did not change significantly with the use of the LDH catalysts. This indicates that the catalyst supports were more suited for improving the lighter pyrolysis oil fractions than the heavier fractions, as a result of the pore widths. Future studies should be conducted on catalyst supports with larger pore sizes to see clearer differences in the heat exchanger oil fractions.

The higher heating values of ESP oils produced using MgAl-LDH catalysts supported by mesoporous silica were significantly higher than that of the non-catalyzed oils. Even though there was an improvement with the MgAl-LDH catalysts, the HHVs were too low for typical fuel applications. This was largely as a result of the high water content in the oils. This can be improved by distilling the oils, removing water using an initial condensation step, or upgrading them further, and thereafter repeating the oil analysis to see if the oils will make viable fuels. Overall, the contents of oxygenated compounds in the pyro-oils, and especially the ESP oils, were reduced by MgAl-LDH and increased by CaAl-LDH. The mesoporous silica supports synthesized at a pH of 7 appeared to yield the greatest catalytic activities for both LDHs.

References

Amonette, J. and Matyas, J. (2017), 'Functionalized silica aerogels for gas-phase purification, sensing, and catalysis: A review', *Microporous and Mesoporous Materials* **250**.

Amutio, M., Lopez, G., Alvarez, J., Olazar, M. and Bilbao, J. (2015), 'Fast pyrolysis of eucalyptus waste in a conical spouted bed reactor', *Bioresource Technology 194 (2015) 225–232* .

Amutio, M., Lopez, G., Artetxe, M., Elordi, G., Olazar, M. and Bilbao, J. (2012), 'Influence of temperature on biomass pyrolysis in a conical spouted bed reactor', *Resources, Conservation and Recycling* **59**, 23–31.

Anoop, E., Ajayghosh, V., Nijil, J. and Cm, J. (2014), 'Evaluation of pulp wood quality of selected tropical pines raised in the high ranges of idukki district, kerala', *Journal of Tropical Agriculture* **52**, 59–66.

Arrabito, G., Domenico, B., Aurelio, P., Giuseppe, O., Andrea, M., Alessio, M., Eugenio, P., Bruno, M. and Pier, G. (2019), 'Layered double hydroxides: A toolbox for chemistry and biology', *Crystals* .

Balat, M., Balat, M., Kırtay, E. and Balat, H. (2009), 'Main routes for the thermo-conversion of biomass into fuels and chemicals. part 1: Pyrolysis systems', *Energy Conversion and Management* **50**, 3147–3157.

Behrens, M., Cross, J. S., Akasaka, H. and Ohtake, N. (2017), 'A study of guaiacol, cellulose and hinoki wood pyrolysis with silica, zro_2, tio_2 and zsm-5 catalysts', *Journal of Analytical and Applied Pyrolysis* **125**, 178–184.

Ben, H., Wu, F., Wu, Z., Han, G., Jiang, W. and Ragauskas, A. (2019), 'A comprehensive characterization of pyrolysis oil from softwood barks', *Polymers* **11**, 1387.

Bhoi, P., Ouedraogo, A., Soloiu, V. and Quirino, R. (2020), 'Recent advances on catalysts for improving hydrocarbon compounds in bio-oil of biomass catalytic pyrolysis', *Renewable and Sustainable Energy Reviews* **121**.

Bing, W., Zheng, L., He, S., Rao, D., Xu, M., Zheng, L., Wang, B., Wang, Y. and Wei, M. (2018), 'Insights on active sites of caal-hydrotalcite as a high-performance solid base catalyst toward aldol condensation', *Catalysis* **8**, 656–664.

Bridgewater, T. (2018), 'Challenges and opportunities in fast pyrolysis of biomass: Part i introduction to the technology, feedstocks and science behind a promising', *Johnson Matthey Technological Review, 2018, 62, (1), 118–130* .

Carlson, T., Tompsett, G., Conner, W. and Huber, G. (2009), 'Aromatic production from catalytic fast pyrolysis of biomass-derived feedstocks', *Topics in Catalysis* **52**, 241–.

Carrier, M., Joubert, J.-E., Dahmen, N., Stahl, R. and Knoetze, H. (2014), 'Inherent process variations between fast pyrolysis technologies: A case study on eucalyptus grandis', *Fuel Processing Technology* **131**, 389–395.

Chen, T., Ku, X., Lin, J. and Ström, H. (2020), 'CFD-DEM Simulation of Biomass Pyrolysis in Fluidized-Bed Reactor with a Multistep Kinetic Scheme', *Energies* **13**, 5358.

Chen, W., Che, Q., Li, S., Liu, Z., Yang, H., Chen, Y., Wang, X., Shao, J. and Chen, H. (2019), 'Recent developments in lignocellulosic biomass catalytic fast pyrolysis: Strategies for the optimization of bio-oil quality and yield', *Fuel Processing Technology* **196**, 106180.

Chen, X., Che, Q., Li, S., Liu, Z., Haiping, Y., Yingquan, C., Wang, X., Shao, J. and Chen, H. (2019), 'Recent developments in lignocellulosic biomass catalytic fast pyrolysis: Strategies for the optimization of bio-oil quality and yield', *Fuel Processing Technology* **196**.

Chen, X., Zhang, K., Xiao, L., Sun, R. and Song, G. (2020), 'Total utilization of lignin and carbohydrates in eucalyptus grandis: an integrated biorefinery strategy towards phenolics, levulinic acid, and furfural', *Biotechnology for Biofuels* **13**.

Corral Valero, M. and Raybaud, P. (2020), 'Computational chemistry approaches for the preparation of supported catalysts: Progress and challenges', *Journal of Catalysis* **391**, 539–547.

Czernik, S. and Bridgwater, T. (2004), 'Overview of applications of biomass fast pyrolysis oil', *Energy* **18**, 590–598.

David, E. (2015), 'Mechanical strength and reliability of the porous materials used as adsorbents/catalysts and the new development trends', *Archives of Materials Science and Engineering* **73**, 5–17.

de Jong, K. P. (2009), *Synthesis of Solid Catalysts*, Wiley-VCH, Weinheim.

Deutschmann, O., Knozinger, H., Kochloefl, K. and Turek, T. (2009), *Heterogenous Catalysis and Solid Catalysts*, Wiley-VCH, Weinheim.

Deutschmann, O., Knözinger, H., Kochloefl, K. and Turek, T. (2011), 'Ullmann's encyclopedia of industrial chemistry heterogeneous catalysis and solid catalysts, 2. development and types of solid catalysts', *Ullmann's Encyclopedia of Industrial Chemistry* .

Eschenbacher, A., Fennell, P. and Jensen, A. (2021), 'A review of recent research on catalytic biomass pyrolysis and low-pressure hydropyrolysis', *Energy Fuels* .

Fahmi, R., Bridgwater, T., Darvell, L., Jones, J., Yates, N., Thain, S. and Donnison, I. (2007), 'The effect of alkali metals on combustion and pyrolysis of lolium and festuca grasses', *Fuel* **86**, 1560–1569.

Fotoohi, B., Kazemzad, M. and Mercier, L. (2018), 'Additive-free synthesis of robust monolithic mesoporous silica support used in catalysis', *Ceramics International* **44**, 20199–20210.

Goh, B., Chong, C. T., Ong, H. C., Seljak, T., Katrašnik, T., Józsa, V., Ng, J.-H., Tian, B., Karmarkar, S. and Veeramuthu, A. (2021), 'Recent advancements in catalytic conversion pathways for synthetic jet fuel produced from bioresources', *Energy Conversion and Management* **251**, 114974.

Heidari, A., Stahl, R., Younesi, H., Rashidi, A., Troeger, N. and Ghoreyshi, A. A. (2014), 'Effect of process conditions on product yield and composition of fast pyrolysis of eucalyptus grandis in fluidized bed reactor', *Journal of Industrial and Engineering Chemistry* **20**, 2594–2602.

Hernández Enciso, W., Lauwaert, J., Van Der Voort, P. and Verberckmoes, A. (2017), 'Recent advances on the utilization of layered double hydroxides (ldhs) and related heterogeneous catalysts in a lignocellulosic-feedstock biorefinery scheme', *Green Chem.* **19**.

Hora, L., Kelbichova, V., Kikhtyanin, O., Bortnovskiy, O. and Kubicha, D. (2014), 'Aldol condensation of furfural and acetone over mgsingle bondal layered double hydroxides and mixed oxides', *Catalysis Today* **223**, 138–147.

Hu, C., Zhang, H., Wu, S. and Xiao, R. (2020), 'Molecular shape selectivity of hzsm-5 in catalytic conversion of biomass pyrolysis vapors: The effective pore size', *Energy Conversion and Management* **210**, 112678.

Hu, X. and Gholizadeh, M. (2019), 'Biomass pyrolysis: A review of the process development and challenges from initial researches up to the commercialisation stage', *Journal of Energy Chemistry* **39**.

Iliopoulou, E., Antonakou, E., Karakoulia, S., Vasalos, I., Lappas, A. and Triantafyllidis, K. (2007), 'Catalytic conversion of biomass pyrolysis products by mesoporous materials: Effect of steam stability and acidity of Al-MCM-41 catalysts', *Chemical Engineering Journal* **134**, 51–57.

Imran, A., Bramer, E. A., Seshan, K. and Brem, G. (2018), 'An overview of catalysts in biomass pyrolysis for production of biofuels', *Biofuel Research Journal* **20**, 872–885.

Jahirul, M., Rasul, M. G., Chowdhury, A. A. and Ashwath, N. (2016), 'Biofuels production through biomass pyrolysis —a technological review', *Energies* **5**, 4952–5001.

Kalogiannis, K., Stefanidis, S., Karakoulia, S., Triantafyllidis, K., Yiannoulakis, H., Mihailof, C. and Lappas, A. (2018), 'First pilot scale study of basic vs acidic catalysts in biomass pyrolysis: Deoxygenation mechanisms and catalyst deactivation', *Applied Catalysis B: Environmental* **238**.

Kan, T., Strezov, V., Evans, T., He, J., Kumar, R. and Lu, Q. (2020), 'Catalytic pyrolysis of lignocellulosic biomass: A review of variations in process factors and system structure', *Renewable and Sustainable Energy Reviews* **134**, 110305.

Katikaneni, S. P. R., Adjaye, D. D. and Bakhshi, N. N. (1995), 'Performance of aluminophosphate molecular sieve catalysts for the production of hydrocarbons from wood-derived and vegetable oils', *Energy Fuels* **9**, 1065–1078.

Ko, E. I. (1999), Sol-gel process, *in* G. Ertl, H. Knözinger and J. Weitkamp, eds, 'Preparation of Solid Catalysts', Wiley-VCH, p. 85.

Kumar, S., Malik, M. and Purohit, R. (2018), 'Synthesis of high surface area mesoporous silica materials using soft templating approach', *Materials Today: Proceedings* **5**, 4128–4133.

Kurdyukov, D., Eurov, D., Kirilenko, D., Kukushkina, J., Sokolov, V., Yagovkina, M. and Golubev, V. (2015), 'High-surface area spherical micro-mesoporous silica particles', *Microporous and Mesoporous Materials* **223**.

Labuschagne, J., Dan, M., Focke, W. and Ofosu, O. (2019), 'Layered double hydroxide derivatives as flame retardants for flexible pvc', *Macromolecular Symposia* **384**, 1800148.

Lappas, A., Samolada, M., Iatridis, D., Voutetakis, S. and Vasalos, I. (2002), 'Biomass pyrolysis in a circulating fluid bed reactor for the production of fuels and chemicals', *Fuel* **81**, 2087–2095.

Loumi, H., Zermane, F., Cheknane, B., Bouchenafa, N., Bouras, O. and Bonilla-Petriciolet, A. (2022), 'Synthesis and characterization of new catalysts grains based on iron(oxy)hydroxides supported on zirconium for the degradation of 4-nitrophenol in aqueous solution', *Adsorption Science Technology* **2022**, 7138770.

Lu, J., Wang, M., Zhang, X., Heyden, A. and Wang, F. (2016), '-o-4 bond cleavage mechanism for lignin model compounds over pd catalysts identified by combination of first-principles calculations and experiments', *ACS Catalysis* **6**.

Luna Murillo, B., Pala, M., Lucini Paioni, A., Baldus, M., Ronsse, F., Prins, W., Bruijnincx, P. and Weckhuysen, B. (2020), 'Catalytic fast pyrolysis of biomass: Catalyst characterization reveals the feed-dependent deactivation of a technical zsm-5-based catalyst', *ACS Sustainable Chemistry Engineering* **9**.

Malucelli, G. (2016), 'Hybrid organic/inorganic coatings through dual-cure processes: State of the art and perspectives', *Coatings* **6**, 10.

Merckel, R. (2014), 'Fast and microwave-induced pyrolysis bio-oil from eucalyptus grandis: Possibilities for upgrading'.

Merckel, R., Heydenrych, M. and Sithole, B. (2020), 'Pyrolysis oil composition and catalytic activity estimated by cumulative mass analysis using py-gc/ms ega-ms', *Energy* **219**, 119428.

Moutsoglou, A., Lawburgh, B. and Lawburgh, J. (2018), 'Fractional condensation and aging of pyrolysis oil from softwood and organosolv lignin', *Journal of Analytical and Applied Pyrolysis* **135**.

Mysore Prabhakara, H., Bramer, E. and Brem, G. (2022), 'Hydrotalcite as a deoxygenation catalyst in fast pyrolysis of biomass for the production of high quality bio-oil', *Journal of Analytical and Applied Pyrolysis* **161**, 105431.

Navarro, R. M., Guil-Lopez, R., Fierro, J. L. G., Mota, N., Jiménez, S., Pizarro, P., Coronado, J. M. and Serrano, D. P. (2018), 'Catalytic fast pyrolysis of biomass over mg-al mixed oxides derived from hydrotalcite-like precursors: influence of mg/al ratio', *Journal of Analytical and Applied Pyrolysis* **134**, 362–370.

Ong, H. C., Chen, W.-H., Singh, Y., Gan, Y. Y., Chen, C.-Y. and Show, P.-L. (2020), 'A state-of-the-art review on thermochemical conversion of biomass for biofuel production: A tg-ftir approach', *Energy Conversion and Management* **209**, 112634.

Panwar, N., Kaushik, S. and Kothari, S. (2011), 'Role of renewable energy sources in environmental protection: A review', *Renewable and Sustainable Energy Reviews* **15**, 1513–1524.

Pedraza, L., Toribio-Cuaya, H., Macías-Bravo, S., González-García, I., Vasquez-Medrano, R. and Favela-Torres, E. (2014), 'Characterization of lignocellulosic biomass using five simple steps', *Journal of Chemical, Biological and Physical Sciences* **4**, 29–47.

Pereira, B., Carneiro, A., Márcia, A., Colodette, J., Oliveira, A. and Fontes, M. (2013), 'Influence of chemical composition of eucalyptus wood on gravimetric yield and charcoal properties', *BioResources* **8**.

Ratnasari, D., Yang, W. and Jönsson, P. (2020), 'Catalytic pyrolysis of lignocellulosic biomass: The influence of the catalyst regeneration sequence on the composition of upgraded pyrolysis oils over a h-zsm-5/al-mcm-41 catalyst mixture', *ACS Omega* **5**, 28992–29001.

Raza, M., Inayat, A., Ahmed, A., Jamil, F., Ghenai, C., Raza Naqvi, S., Shanableh, A., Ayoub, M., Waris, A. and Park, Y.-K. (2021), 'Progress of the pyrolyzer reactors and advanced technologies for biomass pyrolysis processing', *Sustainability* **13**, 11061.

Schubert, U. S. and Hüsing, N. (2019), *Synthesis of Inorganic Materials, 4th Edition*, Wiley.

Schwartz, N., Paulsen, A., Blaise, M., Wagner, A. and Yelvington, P. (2020), 'Analysis of emissions from combusting pyrolysis products', *Fuel* **274**, 117863.

Silverstein, R., Webster, F. and Kiemle, D. (2005), 'Spectrophotometric identification of organic compounds', *John Wiley and Sons* pp. 150–151.

Simatupang, L., Siburian, R., Sitanggang, P., Doloksaribu, M., Situmorang, M. and Marpaung, H. (2018), 'Synthesis and application of silica gel base on mount Sinabung's fly ash for Cd(II) removal with fixed bed column', *Rasayan Journal of Chemistry* **11**, 819–827.

Song, Y., Beaumont, S., Zhang, X., Wilson, K. and Lee, A. (2019), 'Catalytic applications of layered double hydroxides in biomass valorisation', *Current Opinion in Green and Sustainable Chemistry* **22**.

Sun, T.-L., Lei, T.-Z., Li, Z.-F., Wang, Z.-W., Yang, S.-H., He, X.-F., Yue, Z.-H., Gao, Y., Wu, Y.-F. and Shi, X.-G. (2018), 'Optimization of the pyrolysis carbonization of various corn stalk parts in a rotating bed reactor based on energy yield', *Journal of Biobased Materials and Bioenergy* **12**, 378–386.

Sun, T., Li, Z., Zhang, Z., Wang, Z., Yang, S., Yang, Y., Wang, X., Liu, S., Zhang, Q. and Lei, T. (2020), 'Fast corn stalk pyrolysis and the influence of catalysts on product distribution', *Bioresource Technology* **301**, 122739.

Tabish, M., Yasin, G., Anjum, M., Malik, M., Zhao, J., Yang, Q., Manzoor, S., Murtaza, H. and Khan, W. (2020), 'Reviewing the current status of layered double hydroxide-based smart nanocontainers for corrosion inhibiting applications', *Journal of Materials Research and Technology* **10**.

Wang, H., Zhang, C., He, H. and Wang, L. (2012), 'Glucose production from hydrolysis of cellulose over a novel silica catalyst under hydrothermal conditions', *Journal of environmental sciences (China)* **24**, 473–8.

Wang, L., Wang, Y., Wang, X., Feng, X., Ye, X. and Fu, J. (2018), 'Small-sized mg–al ldh nanosheets supported on silica aerogel with large pore channels: Textural properties and basic catalytic performance after activation', *Nanomaterials* **8**, 113.

Wang, Y., Zhang, F., Xu, S., Wang, X., Evans, D. and Duan, X. (2008), 'Preparation of layered double hydroxide microspheres by spray drying', *Industrial Engineering Chemistry Research - IND ENG CHEM RES* **47**.

Wei, Y., Yang, W. and Yang, Z. (2022), 'An excellent universal catalyst support-mesoporous silica: Preparation, modification and applications in energy-related reactions', *International Journal of Hydrogen Energy* **47**.

Yildiz, G., Ronsse, F., Van Duren, R. and Prins, W. (2016), 'Challenges in the design and operation of processes for catalytic fast pyrolysis of woody biomass', *Renewable and Sustainable Energy Reviews* **57**, 1596–1610.

Zhang, L., Bao, Z., Xia, S., Lu, Q. and Walters, K. (2018), 'Catalytic pyrolysis of biomass and polymer wastes', *Catalysts* **8**, 659.

A Exploratory catalyst formulation

A.1 Variations in concentrations of sodium silicate precursor solution

In the initial phases of exploratory catalyst formulation, the intention was to maximise the yield of the silica support by using the maximum concentration of sodium silicate in the precursor. The same procedure was followed as the final procedure, but a precursor sodium silicate solution of 20% was used. The catalyst particles produced using this method were more, as expected. However, they were brittle enough to crush by hand. The particles were especially easily crushed during and after washing. The reason for this is likely that when the silanol groups were formed and the gels underwent drying, a large portion of the silicate recrystallised into sodium silicate molecules, which were trapped inside and between the silica matrix structure. These sodium silicate molecules acted as weak points in the matrix, making the matrix easy to crush. In addition, the sodium silicate dissolves in water, which is why washing made the particles even weaker.

This was easily remedied through the lowering of the precursor solution to around 1% sodium silicate. However, the yield of gel was found to be extremely low for the quantity needed to perform various analyses and experiments. By trial and error, an increased concentration of 9% was found to yield a good trade-off between particle strength and yield.

A.2 Acid addition

There is very little information in the literature about the manner in which acid is added to the precursor solution to initiate gel formation. Therefore, this process inolved trial-and-error. The same initial procedure was formed as in the final procedure (namely, precursor production). At first, this was followed by sudden addition of the entire quantity of concentrated (98%) acid. When this was done, the polymerisation reaction happened so quickly that the precursor mixture almost instantly became a slurry consisting of small, solid pieces, which were brittle and not of a gel consistency. The reason for this likely has to do with the nature of the bonds that were formed, and the silica matrix morphology.

This was fixed by adding the acid dropwise until the decreasing pHs of 5, 7 and 9 were reached. The dropwise addition resulted in a much more gel-like result. However, it was

observed that the gels seemed to be filled with tiny bubbles. It was realised that these bubbles were carbon dioxide that was formed through the reaction of the LDH with the concentrated acid added to the mixture. This was not desired, because this meant that the LDH layers were being destroyed. This problem was easily fixed by reducing the added acid solution concentration to 20%, without adversely affecting the gel formation reaction.

A.3 Variations in LDH loading

Initially, the intention was to maximise the loading of LDH in the catalyst particles. The same method was used as the final method, but with larger quantities of LDH in comparison to the precursor solution. It was found that amounts of LDH larger than 20% yielded soft, brittle, chalky particles that left a powder residue when handled. This means that the LDH was not adequately entrapped within the silica matrix as a result of the high loading. Upon trial-and-error, it was found that concentrations of LDH below 10% were significantly harder and left no residue.

A.4 Variations in gel washing procedures

After the first few sets of gels were produced by following the finalised procedures, attempts were made to wash the gels as per examples from literature. Initially, the gels were washed immediately after they were synthesised so that they could proceed to drying. It was soon found that these gels were extremely brittle once dried. After examining more literature, it was determined that the gels needed to 'age' for at least 30 minutes after being synthesised. The reason for this is that the polymerisation reaction still continues beyond the initial rapid gel formation, and additional silanol linkages continue to form within the silica matrix for some time after the synthesis step. This makes the final gel and the subsequent catalyst particles much stronger.

After this finding, it was decided to observe the effect of not washing the gels at all. The presumption was that this would result in even more silanol linkages, creating even stronger particles. However, the dried gels were found to form an abundance of visible salt crystals, which were the water-soluble salts (sodium sulphate) produced as a by-product of the polymerisation reaction. In addition, the salts caused the dried gels to crumble with almost no effort. It was determined that, for the same reasons that excess sodium silicate produces weak particles, the production of these salts needs to be avoided. Therefore, repeated rounds

of washing with distilled water to dissolve and remove these salt is crucial.

A.5 Variations in the formation of catalyst particles

Numerous methods of forming the successful gels into viable particles were investigated. The first method was simply the formation of the gels into lines, which were chopped into small pellets. This proved to be inefficient without specialised cutting/chopping equipment, and was labour-intensive for the number of particles produced. This method was therefore discarded.

A novel method described in some literature was attempted, whereby droplets of the still wet gels were injected onto plastic sheets, forming round, droplet-shaped particles that would presumably become more spherical as they dried. In principle, this was successful, but was laborious and produced many particles with sharp edges. This was seen as undesired, because the sharp edges could act as weak points when exposed to abrasion in the fluidised bed, increasing the catalyst friability. This method was discarded.

An attempt was made to produce small, cylindrical-shaped particles by extruding the still fairly wet gels through synringes into lines, followed by chopping into pellets and further drying. Although there were a few successful sets of catalysts, the process was extremely laborious. Additionally, the consistencies and ease of extrusion was hugely dependent on many variables, including the formulations and the drying process. This method was thus also discarded, and replaced with the more successful and more efficient method of rolling using sieve trays.

B Detailed GC/MS Results

B.1 ESP oil composition

B.2 Heat exchanger oil organic fraction composition

Table 6: GC/MS results of compounds with highest peak area percentages in the ESP oils

Compound	Peak Area (%) - No catalyst	Peak Area (%) - Silica support	Peak Area (%) - MgAl-LDH (1)	Peak Area (%) - MgAl-LDH (2)	Peak Area (%) - MgAl-LDH (3)	Peak Area (%) - CaAl-LDH (1)	Peak Area (%) - CaAl-LDH (2)	Peak Area (%) - CaAl-LDH (3)
Hydrazinecarboxamide	0.33	7.14	0.70	0.19	0.28	0.82	6.14	6.96
Acetone	1.69	0.84	0.65	0.71	1.01	10.98	7.43	1.08
2-methyl pentane	16.79	20.28	21.47	21.32	21.85	15.80	15.21	17.27
3-methyl pentane	17.21	19.03	21.16	21.22	20.82	15.11	11.91	13.57
Methylcyclopentane	12.39	12.29	10.17	12.17	9.63	10.03	11.87	8.21
2-methyl hexane	3.19	1.68	2.72	2.4	2.62	0.51	1.08	3.36
3-methyl hexane	1.64	1.19	1.40	1.26	1.44	3.4	3.73	0.63
Heptane	0.32	0.24	0.29	0.32	0.27	0.03	0.20	4.49
Toluene	0.47	0.59	0.39	0.25	0.37	0.92	1.24	0.16
2-amino oxazolidin	0.22	0.198	0.13	0.09	0.12	0.39	0.47	0.66
3-furadeldehyde	0.09	0.14	0.00	0.00	0.06	0.21	0.04	0.40
Furfural	1.64	2.15	1.17	0.54	0.97	3.23	4.11	3.19
Phenethyl-β-phenol	0.25	0.29	0.15	0.10	0.13	0.28	0.48	0.26
Phenol	2.99	2.03	1.04	0.40	0.67	2.34	2.33	2.25
2-methyl phenol	1.47	1.3	0.63	0.24	0.45	1.45	1.61	1.55
3-methyl phenol	2.60	2.25	1.19	0.05	0.74	2.74	2.84	2.59
Butyrolactone	0.58	0.85	0.46	0.02	0.35	1.58	1.83	0.11
Benzaldehyde	0.21	0.26	0.15	0.06	0.1	0.21	0.41	0.34
Dimethyl 2,6-phenol	0.44	0.52	0.28	0.12	0.21	0.15	0.25	0.06
Ethylphenol	0.29	0.03	0.07	0.04	0.08	0.17	0.19	0.12
Dimethyl 2,5-phenol	0.93	0.01	0.45	0.15	0.26	1.04	0.02	0.44
Napthalene	0.59	0.49	0.15	0.38	0.71	0.23	0.35	0.18
Trimethyl 2,3,5-phenol	0.53	0.5	0.06	0.08	0.14	0.35	0.91	6.25
Ethyl 2,4-methylphenol	0.55	0.76	0.03	0.11	0.21	1.14	1.03	0.36
Hexane	31.85	31.23	34.67	37.38	36.09	26.06	22.74	23.96

Table 7: GC/MS results of compounds with highest peak area percentages in the heat exchanger oil organic fractions

Compound	Peak Area (%) - No catalyst	Peak Area (%) - Silica support	Peak Area (%) - MgAl-LDH (1)	Peak Area (%) - MgAl-LDH (2)	Peak Area (%) - MgAl-LDH (3)	Peak Area (%) - CaAl-LDH (1)	Peak Area (%) - CaAl-LDH (2)	Peak Area (%) - CaAl-LDH (3)
Methanol	19.88	18.34	30.58	31.32	20.51	27.71	39.42	36.93
Acetic acid	5.43	2.25	6.29	7.11	7.19	6.27	5.64	9.28
Methyl glyoxal	4.93	5.53	3.40	3.05	4.40	10.55	7.66	4.16
Hexane	3.75	1.80	0.97	0.79	0.87	1.32	1.45	2.32
Furfural	3.75	5.48	3.73	3.78	4.46	4.29	3.48	4.39
1,2-epoxy-3-propyl acetate	3.31	5.20	3.26	2.89	2.92	4.14	2.34	2.85
2,3-dihydroxy-propanal	2.98	3.66	3.50	2.53	2.50	1.78	1.88	3.88
Succinaldehyde	2.48	3.06	1.96	2.19	2.25	2.02	1.17	1.16
Phenol	2.13	2.83	0.08	2.17	0.12	0.11	1.19	2.32
Butyrolactone	1.94	2.41	2.20	2.31	1.89	1.76	1.55	1.88
Catechol	1.56	2.14	1.81	3.47	1.09	0.58	0.50	0.99
3-methyl phenol	1.55	1.84	1.83	1.79	1.59	1.25	1.08	1.33
4-ethyl 1,3-dioxalone	1.16	0.52	1.51	1.25	1.45	1.81	1.34	1.23
3-methyl pentane	1.04	0.59	0.63	0.42	0.95	0.65	1.19	1.97
3-amino-2-oxazolidinone	0.97	1.19	0.87	1.12	0.99	0.91	0.75	0.85
2-methyl phenol	0.91	1.80	0.98	1.15	1.00	0.75	0.18	1.94
2-octenoic acid	0.85	0.32	2.90	1.37	1.60	2.73	0.29	1.45
2-methyl pentane	0.82	0.55	0.59	0.38	0.38	0.61	0.68	1.94
4-methyl 1,2-benzenediol	0.80	0.81	0.63	1.25	0.34	0.07	0.30	0.36
3-ethyl phenol	0.44	0.51	1.83	1.79	0.05	0.28	0.29	1.33

C Python Code

C.1 FTIR peak deconvolution

```
from numpy import trapz
from scipy.special import erf
import pandas as pd
import numpy as np
from scipy.optimize import curve_fit
import matplotlib.pyplot as plt

for k in range(len(spectra_list)):
    data = pd.read_csv(spectra_list[k]) #retrieving spectrum data
    data_array = np.asarray(data).T #transposing data
    wavenumbers, absorbances = data_array

    def gaussian_with_1_peak(x, a0, a1, a2):
        function = a0*np.exp(-((x-a1)**2)/(2*(a2**2))) #single gaussian curve
        return function

    def gaussian_with_3_peaks(m, a0_1, a1_1, a2_1, a0_2, a1_2, a2_2, a0_3, a1_3,
        a2_3):
        #a0_1 = parameters[0] # peak area
        #a1_1 = parameters[1] # elution time
        #a2_1 = parameters[2] # width of gaussian
        function1 = gaussian_with_1_peak(m, a0_1, a1_1, a2_1)
        function2 = gaussian_with_1_peak(m, a0_2, a1_2, a2_2)
        function3 = gaussian_with_1_peak(m, a0_3, a1_3, a2_3)
        return function1 + function2 + function3 #superimposed gaussian curves
            for each peak

    wavenumbers_1600 = wavenumbers[4275:5000] #retrieving data for peak around
        1650cm-1
    absorbances_1600 = absorbances[4275:5000]
    wavenumbers_3300 = wavenumbers[0:3075] #retrieving data for peak around
        3400cm-1
    absorbances_3300 = absorbances[0:3075]
```

```
p0_list = [[0.1, 1600, 0.1, 0.1, 1650, 0.1, 0.1, 1720, 0.1], [0.1, 2900, 0.1,
    0.1, 3200, 0.1, 0.1, 3400, 0.1]] #initial guesses
wavenumbers_list = [wavenumbers_1600, wavenumbers_3300]
absorbances_list = [absorbances_1600, absorbances_3300]
legend_labels = [['C=C (alkenes) peak', '-OH (water) peak', 'C=O (carbonyl)
    peak'], ['C-H (alkanes) peak', 'O-H (alcohols) peak', 'O-H (water) peak']]

fig, axes = plt.subplots(nrows=1, ncols=2, figsize=(14, 4))

for i in range(len(wavenumbers_list)):
    popt, pcov = curve_fit(gaussian_with_3_peaks, wavenumbers_list[i],
        absorbances_list[i], p0_list[i], bounds=((0, -np.inf, -np.inf, 0,
        -np.inf, -np.inf, 0, -np.inf, -np.inf), (np.inf, np.inf, np.inf,
        np.inf, np.inf, np.inf, np.inf, np.inf, np.inf))) #fitting the peaks
        to three deconvoluted peaks

    axes[i].plot(wavenumbers_list[i], absorbances_list[i],
        label=data_label[k])
    axes[i].plot(wavenumbers_list[i],
        gaussian_with_3_peaks(wavenumbers_list[i], popt[0], popt[1], popt[2],
        popt[3], popt[4], popt[5], popt[6], popt[7], popt[8]),
        label='Superimposed fit') #displaying overall fit
    axes[i].plot(wavenumbers_list[i],
        gaussian_with_1_peak(wavenumbers_list[i], popt[0], popt[1], popt[2]),
        label=legend_labels[i][0]) #displaying first peak
    axes[i].plot(wavenumbers_list[i],
        gaussian_with_1_peak(wavenumbers_list[i], popt[3], popt[4], popt[5]),
        label=legend_labels[i][1]) #displaying second peak
    axes[i].plot(wavenumbers_list[i],
        gaussian_with_1_peak(wavenumbers_list[i], popt[6], popt[7], popt[8]),
        label=legend_labels[i][2]) #displaying third peak
    axes[i].legend()
```

C.2 Water content determination

```
#following on from previous code
if (i==0):
```

```
        waterpeak1_area = trapz([z for z in
            gaussian_with_1_peak(wavenumbers_list[i], popt[3], popt[4],
            popt[5])], dx=1) #calculating area of middle peak for 1650cm-1
    if (i==1):
        waterpeak2_area = trapz([z for z in
            gaussian_with_1_peak(wavenumbers_list[i], popt[6], popt[7],
            popt[8])], dx=1) #calculating area of the last peak for 3400cm-1

axes[0].set_ylabel('Absorbance', fontsize=12)
axes[0].set_xlabel("Wavenumber (cm$^{-1}$)", fontsize=12)
axes[1].set_ylabel('Absorbance', fontsize=12)
axes[1].set_xlabel("Wavenumber (cm$^{-1}$)", fontsize=12)
fig.savefig(file_savename_list[k], dpi=1200, bbox_inches='tight') #saving
    plot image

print(waterpeak1_area, waterpeak2_area)
```